Supporting Information

Frustrated Lewis Pair-Ligated Tetrelenes

Alvaro A. Omaña,[a] Brandon L. Frenette,[a] Eike Dornsiepen,[a] Ryo Kobayashi,[b] Michael J. Ferguson,[a] Takeaki Iwamoto,[b] and Eric Rivard[a,*]

[a]*Department of Chemistry, University of Alberta, 11227 Saskatchewan Drive, Edmonton, Alberta, Canada T6G 2G2*
[b]*Department of Chemistry, Graduate School of Science, Tohoku University, Aoba-ku, Sendai 980-8578, Japan*

Table of Contents

1. Single crystal X-ray structure determinations

Appropriate X-ray quality crystals were coated with a small amount of hydrocarbon oil (Paratone-N) and removed from the glovebox in a vial. Crystals were quickly mounted onto a glass fiber and placed in a low temperature stream of nitrogen on the X-ray diffractometer. All data was collected using a Bruker APEX II CCD detector/D8 or PLATFORM diffractometer using Mo Kα (0.71073 Å) or Cu Kα (1.54178 Å) radiation, with the crystals cooled to -80 °C or -100 °C. For [^{i}Pr$_2$PCH$_2$(C$_6$H$_4$)BMes$_2${CH$_2$}] (**13**), 45 second exposures were needed to collect high quality crystallographic data. The data was corrected for absorption through Gaussian integration from the indexing of crystal faces.[S1] Crystal structures were solved using intrinsic phasing (SHELXT)[S2] and refined using SHELXL-2014.[S3] For [PB{CH$_2$}] (**7**), [{(THF)$_3$Li}^{i}PrP(C$_6$H$_4$)BCy$_2${CH$_2$}] (**8**), [^{i}Pr$_2$PCH$_2$(C$_6$H$_4$)Li(OEt$_2$)]$_2$ (**10**), **^{CH2}PB** and [^{i}Pr$_2$PCH$_2$(C$_6$H$_4$)BMes$_2${CH$_2$}] (**13**), Olex2 was used as a Graphical User Interface (GUI).[S4] The assignment of hydrogen atom positions are based on the *sp*^{2}- or *sp*^{3}-hybridization geometries of their attached carbon atoms and were given thermal parameters 20 % greater than those of their parent atoms. Molecular structures are shown with thermal ellipsoids at a 30% probability and have been generated using SHELXP. All crystallographic information files (.cifs) were deposited within the Cambridge Crystallographic Data Centre (CCDC) database.

Table S1. X-ray crystallographic data for [PB{$SiBr_2$}] (**5**), [PB{AgOTf}]$_2$, and [PB{CH_2}] (**7**).

Compound	**5**	**[PB{AgOTf}]$_2$**	**7**
Formula	$C_{24}H_{40}BBr_2PSi$	$C_{64}H_{96}Ag_2B_2F_6O_6P_2S_2$	$C_{25}H_{42}BP$
Formula weight	558.25	1438.82	384.36
Crystal system	Monoclinic	Triclinic	Monoclinic
Space group	*$P2_1/c$ (No. 14)*	*$P\bar{1}$ (No. 2)*	*$P2_1/c$ (No. 14)*
Crystal dimensions (mm)	0.15×0.12×0.06	0.17×0.15×0.04	0.154×0.113×0.045
a (Å)	9.9653(2)	11.0509(3)	10.5854(3)
b (Å)	15.4219(4)	11.8386(3)	9.8043(2)
c (Å)	17.1801(4)	14.3836(4)	22.5734(5)
α (°)	90	99.1129(11)	90
β (°)	105.5652(13)	105.9672(11)	91.2950(10)
γ (°)	90	108.6188(9)	90
V (Å^3)	2586.70(10)	1650.69(8)	2342.12(10)
Z	4	1	4
ρ (g/cm^3)	1.433	1.447	1.090
Abs coeff (mm^{-1})	5.053	6.350	1.058
T (°C)	–100	–100	–80
$2\theta_{max}$ (°)	140.41	148.16	147.81
Total data	13910	72300	88291
Unique data	4905 (0.0260)	6441 (0.0333)	4607 (0.0637)
Obs data [I>2σ(I)][a]	4172	6261	4070
Params	262	445[b]	496[c,d]
R_1 [I>2σ(I)][a]	0.0444[a]	0.0263[b]	0.0479[c,d]
wR_2 [all data][a]	0.1394	0.0725	0.1356
Max/min Δρ (e$^-$ Å^{-3})	1.441/-1.029	0.770/-0.521	0.87/-0.34

[a] $R_1 = \Sigma||F_o| - |F_c||/\Sigma|F_o|$; $wR_2 = [\Sigma w(F_o^2 - F_c^2)^2/\Sigma w(F_o^4)]^{1/2}$.

[b] The disordered cyclohexyl group (atoms C21A to C26A and C21B to C26B) were restrained to have approximately the same bond lengths by using the SHELXL **SADI** instruction on the following: B1–C21A and B1–C21B; all C–C distances. Additionally, the anisotropic displacement parameters were restrained by use of the SHELXL **SIMU** instruction. Finally, the disordered solvent toluene molecule was constrained to have an idealized phenyl group, the methyl carbon to *ipso*-carbon distance was restrained to be approximately 1.50 Å by use of a SHELXL **DFIX** instruction, and the angles about the ipso carbon atoms were restrained to be approximately 120°. Further, the anisotropic displacement parameters of carbon atoms of the major orientation of the toluene were restrained by use of the SHELXL **RIGU** instruction.

[c] Data were collected with the detector set at three different positions. Low-angle (detector 2θ = –33°) data frames were collected using a scan time of 5 s, medium-angle (detector 2θ = 75°) frames using a scan time of 5 s, and high-angle (detector 2θ= 117°) frames using a scan time of 10 s.

[d]Due to whole molecule disorder, molecule was split into two parts (using **PART** keywords); both refined anisotropically. **SIMU**, **RIGU** and **DELU** restraints were added, alongside **SAME** P1 > C25.

Table S2. X-ray crystallographic data for [{(THF)$_3$Li}^{i}PrP(C$_6$H$_4$)BCy$_2${CH$_2$}] (**8**), [^{i}Pr$_2$PCH$_2$(C$_6$H$_4$)Li(Et$_2$O)]$_2$ (**10**), and ^{CH2}**PB**.

Compound	**8**	**10•Et$_2$O**	^{CH2}**PB**
Formula	$C_{34}H_{59}BLiO_3P$	$C_{34}H_{56.34}Li_2O_2P_2$	$C_{25}H_{42}BP$
Formula weight	564.53	572.95	384.36
Crystal system	Orthorhombic	Monoclinic	Monoclinic
Space group	*P2$_1$2$_1$2$_1$ (No. 19)*	*P2$_1$/n*	*P2$_1$/c (No. 14)*
Crystal dimensions (mm)	0.235×0.173×0.132	0.174×0.147×0.061	0.065×0.164×0.253
a (Å)	9.9428(10)	12.7778(6)	10.7112(4)
b (Å)	16.8849(17)	18.1916(8)	11.6101(4)
c (Å)	20.512(2)	15.8870(7)	18.4751(6)
α (°)	90	90	90
β (°)	90	95.1640(10)	90.8680(10)
γ (°)	90	90	90
V (Å^3)	3443.6(6)	3676.1(3)	2297.28(14)
Z	4	4	4
ρ (g/cm^3)	1.089	1.043	1.111
Abs coeff (mm^{-1})	0.110	0.144	0.127
T (°C)	–80	–100	–100
$2\theta_{max}$ (°)	102.76	102.9	107.6
Total data	28282	56424	26118
Unique data	6531 (0.0730)	7023 (0.0715)	4835 (0.0397)
Obs data [I>2σ(I)][a]	4451	7023	3947
Params	410[c]	393[b]	248
R_1 [I>2σ(I)][a]	0.0579[d]	0.0607[b]	0.0377
wR_2 [all data][a]	0.1595	0.1769[b]	0.0997
Max/min Δρ (e$^-$ Å^{-3})	0.42/-0.26	0.74/-0.48	0.31/-0.22

[a] $R_1 = \Sigma||F_o| - |F_c||/\Sigma|F_o|$; $wR_2 = [\Sigma w(F_o^2 - F_c^2)^2/\Sigma w(F_o^4)]^{1/2}$.

[b] The disorder in the coordinated Et$_2$O solvent molecules for **10** could not be fully resolved by splitting into parts, as they are disordered over more than three locations. Thus, only **SIMU**, **RIGU**, **DELU** restraints were applied to the Et$_2$O molecules.

[c] Due to disordered THF molecules, **RIGU**, **SADI** and **EADP** restraints were used for C23 to C26, C31 to C34.

[d] Refined as an inversion twin: $I_c = (1-x)I_s^+ + xI_s^-$. The Flack parameter ($x$) was determined to be 0.29(19); therefore, the absolute configuration of **9** cannot be conclusively determined and it must be considered a racemic mixture.

Table S3. X-ray crystallographic data for [^{i}Pr$_2$PCH$_2$(C$_6$H$_4$)BMes$_2${CH$_2$}] (**13**):

Compound	**13**
Formula	$C_{32}H_{44}BP$
Formula weight	470.45
Crystal system	Monoclinic
Space group	*P2$_1$/n*
Crystal dimensions (mm)	0.213×0.196×0.170
a (Å)	10.230(2)
b (Å)	19.008(4)
c (Å)	14.985(4)
α (°)	90
β (°)	102.935(4)
γ (°)	90
V (Å^3)	2840.0(12)
Z	4
ρ (g/cm^3)	1.100
Abs coeff (mm^{-1})	0.114
T (°C)	–80
2θ$_{max}$ (°)	104.4
Total data	22944
Unique data	5632 (0.0430)
Obs data [I>2σ(I)][a]	5632
Params	393[b]
R$_1$ [I>2σ(I)][a]	0.0486
wR$_2$ [all data][a]	0.1226
Max/min Δρ (e$^-$ Å^{-3})	0.39/-0.24

[a] $R_1 = \Sigma||F_o| - |F_c||/\Sigma|F_o|$; $wR_2 = [\Sigma w(F_o^2 - F_c^2)^2/\Sigma w(F_o^4)]^{1/2}$.

[b] Disorder within one of the mesityl rings (C15 – C23) was modeled by splitting into two parts, and the site occupancies [*s.o.f.* 0.612(18)] were determined using an isotropic model and freely refined. Atom distances within the disordered mesityl ring were restrained to be approximately equal with the **SADI** command; displacement parameters were also restrained using the enhanced rigid bond restraint (**RIGU**).

2. NMR Spectra

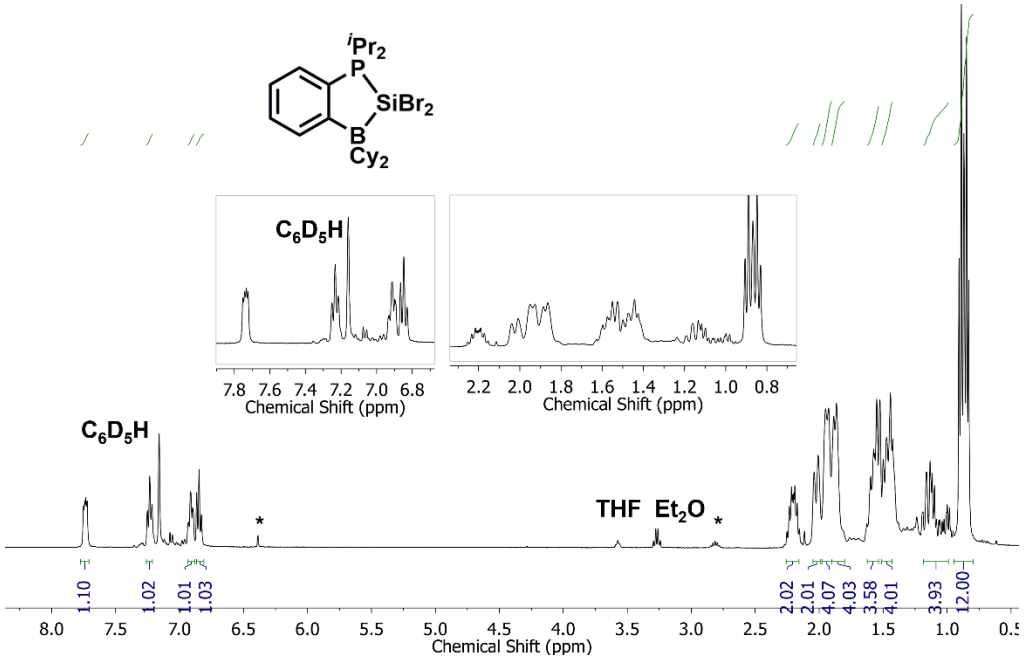

Figure S1. ^{1}H NMR spectrum of [PB{$SiBr_2$}] (**5**) in C_6D_6. Peaks labelled with an asterisk (*) are consistent with the literature data for IPr•$SiBr_2$.[S5]

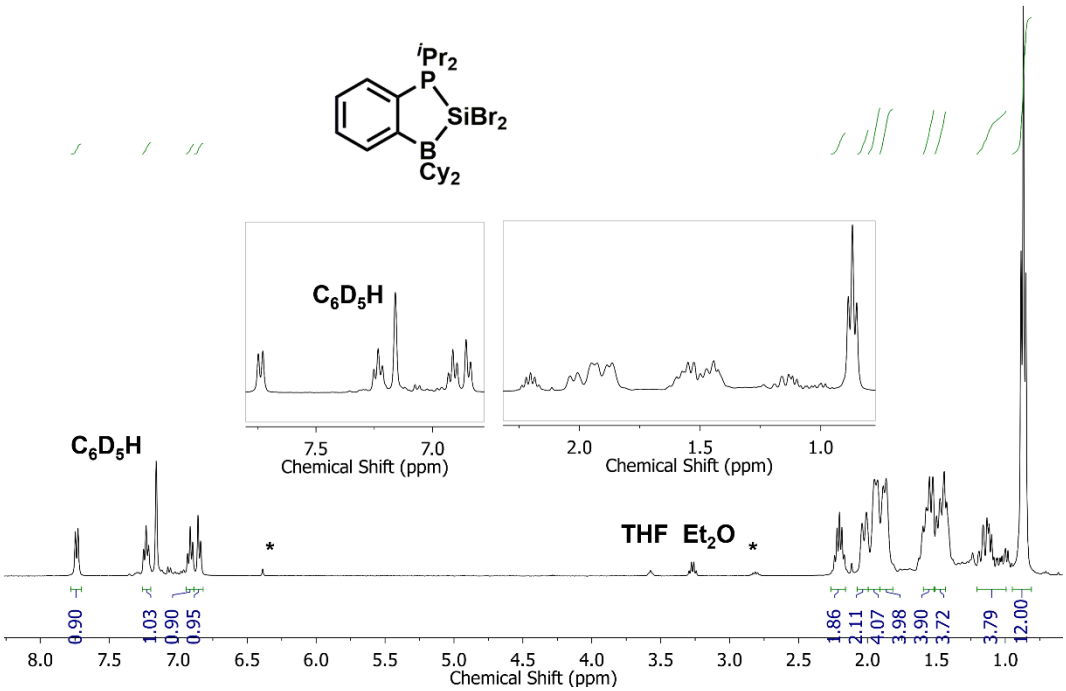

Figure S2. ^{1}H{^{31}P} NMR spectrum of [PB{$SiBr_2$}] (**5**) in C_6D_6. Peaks labelled with an asterisk (*) are consistent with the literature data for IPr•$SiBr_2$.[S5]

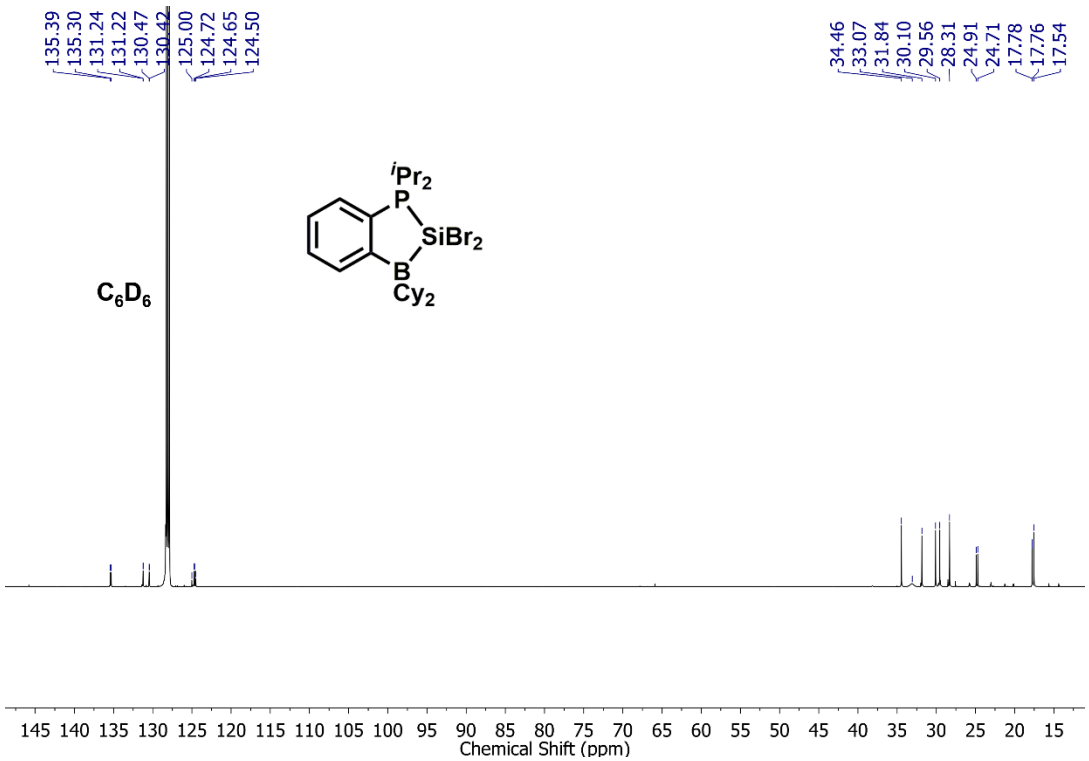

Figure S3. $^{13}C\{^{1}H\}$ NMR spectrum of [PB{$SiBr_2$}] (**5**) in C_6D_6.

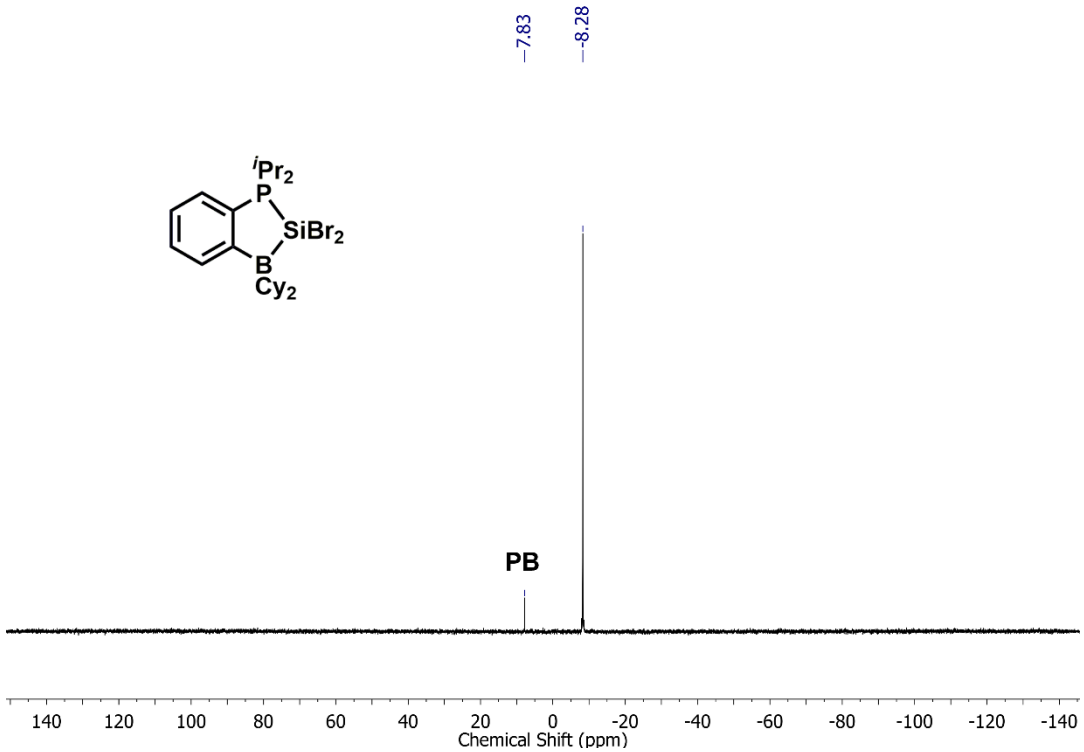

Figure S4. $^{31}P\{^{1}H\}$ NMR spectrum of [PB{$SiBr_2$}] (**5**) in C_6D_6.

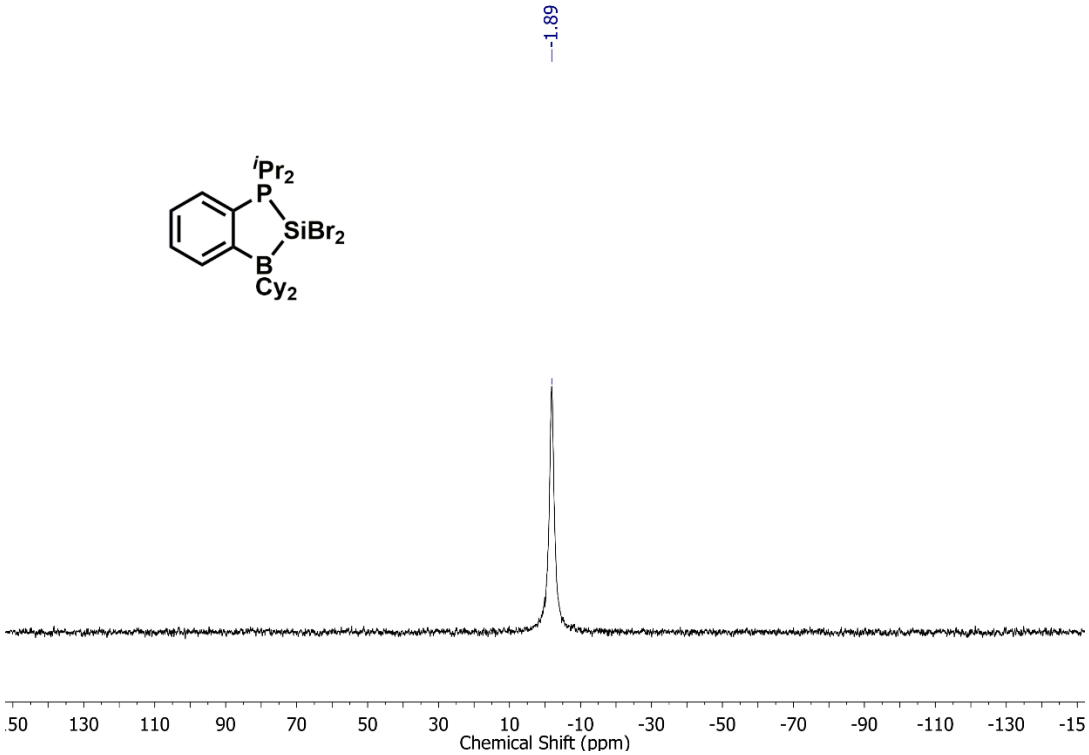

Figure S5. $^{11}B\{^{1}H\}$ NMR spectrum of [PB{$SiBr_2$}] (**5**) in C_6D_6.

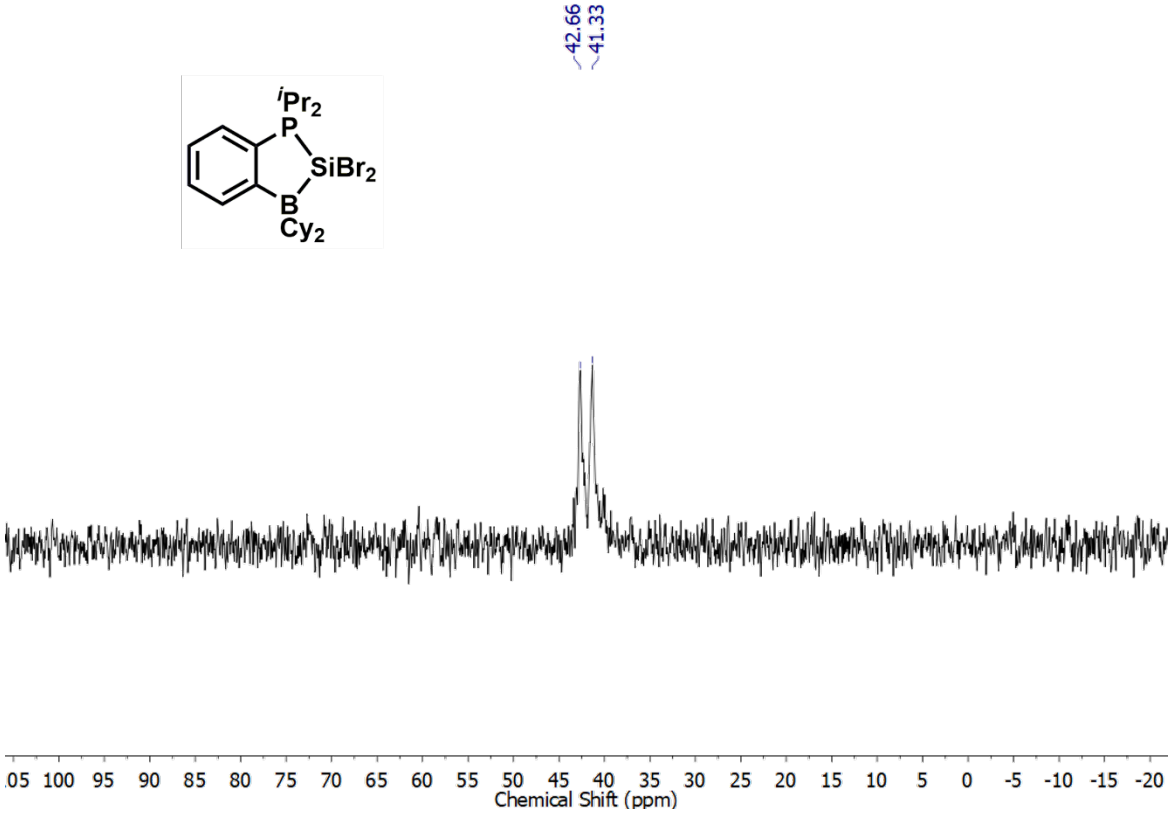

Figure S6. $^{29}Si\{^{1}H\}$ NMR spectrum of [PB{$SiBr_2$}] (**5**) in C_6D_6.

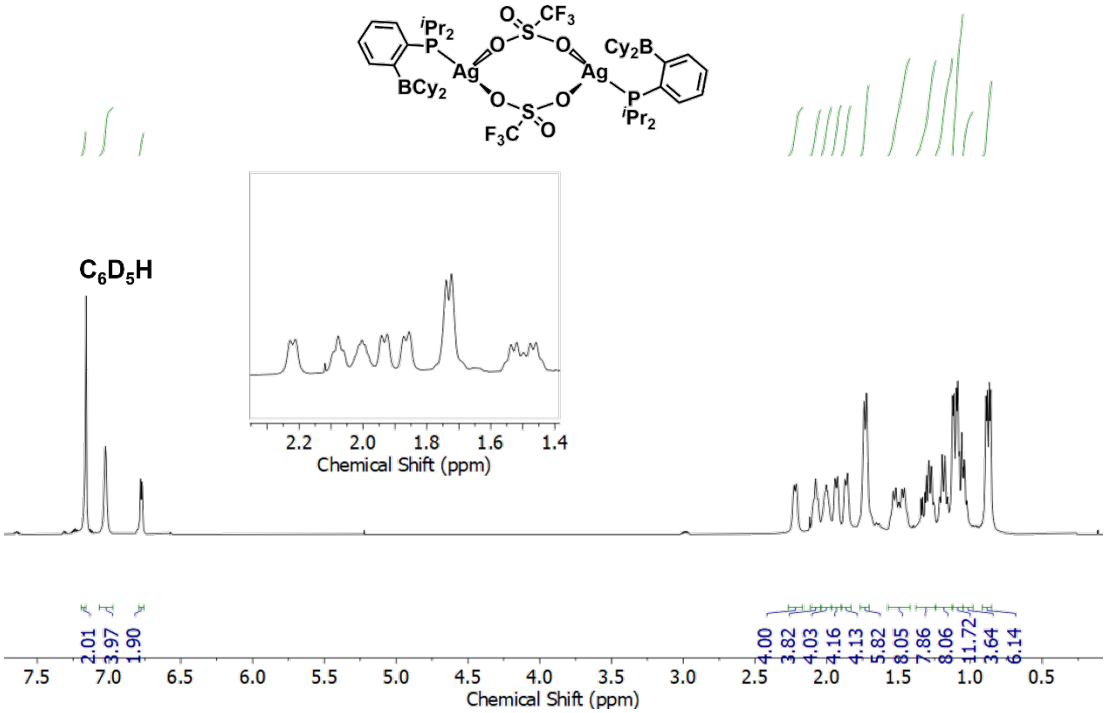

Figure S7. ^{1}H NMR spectrum of $[PB\{AgOTf\}]_2$ in C_6D_6.

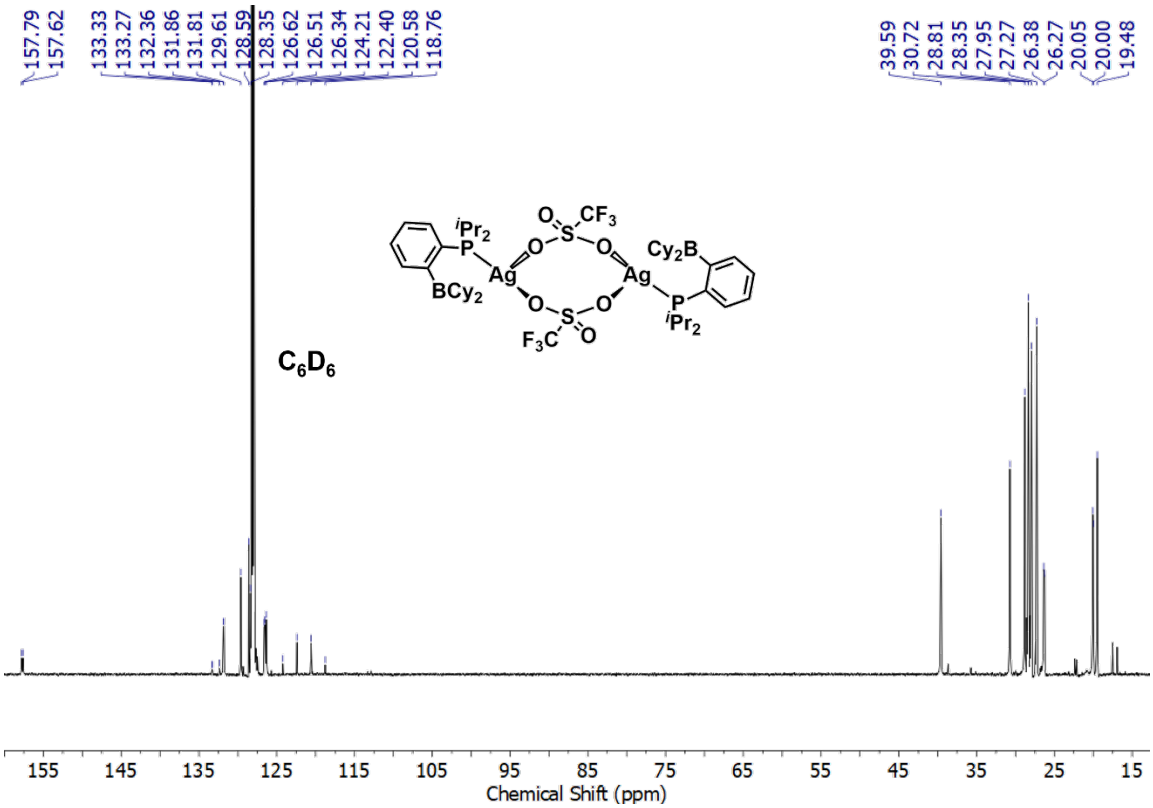

Figure S8. $^{13}C\{^{1}H\}$ NMR spectrum of $[PB\{AgOTf\}]_2$ in C_6D_6.

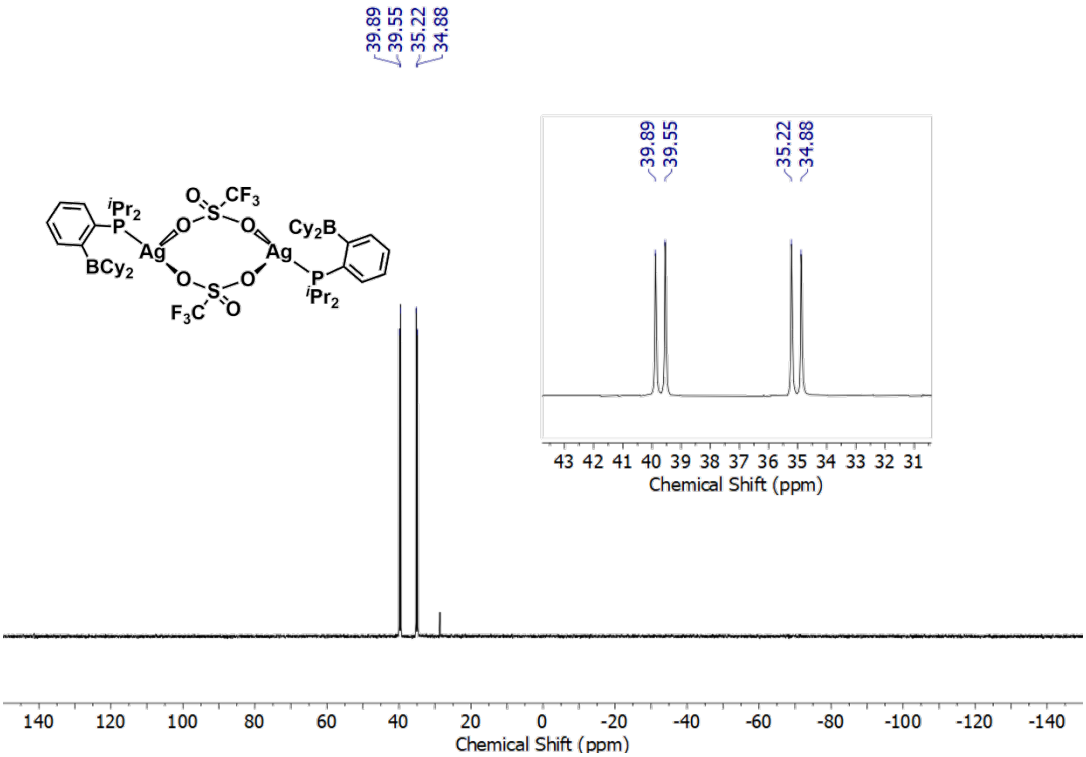

Figure S9. $^{31}P\{^{1}H\}$ NMR spectrum of $[PB\{AgOTf\}]_2$ in C_6D_6. The ^{31}P resonance near 23 ppm is from an unknown impurity.

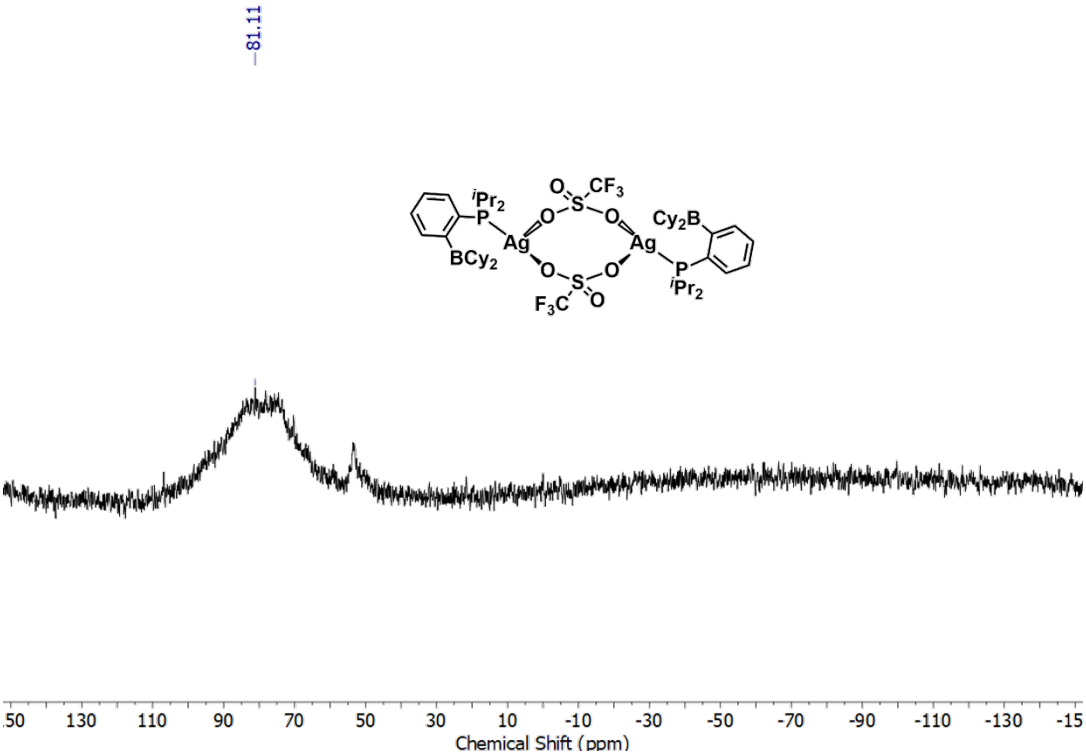

Figure S10. $^{11}B\{^{1}H\}$ NMR spectrum of $[PB\{AgOTf\}]_2$ in C_6D_6.

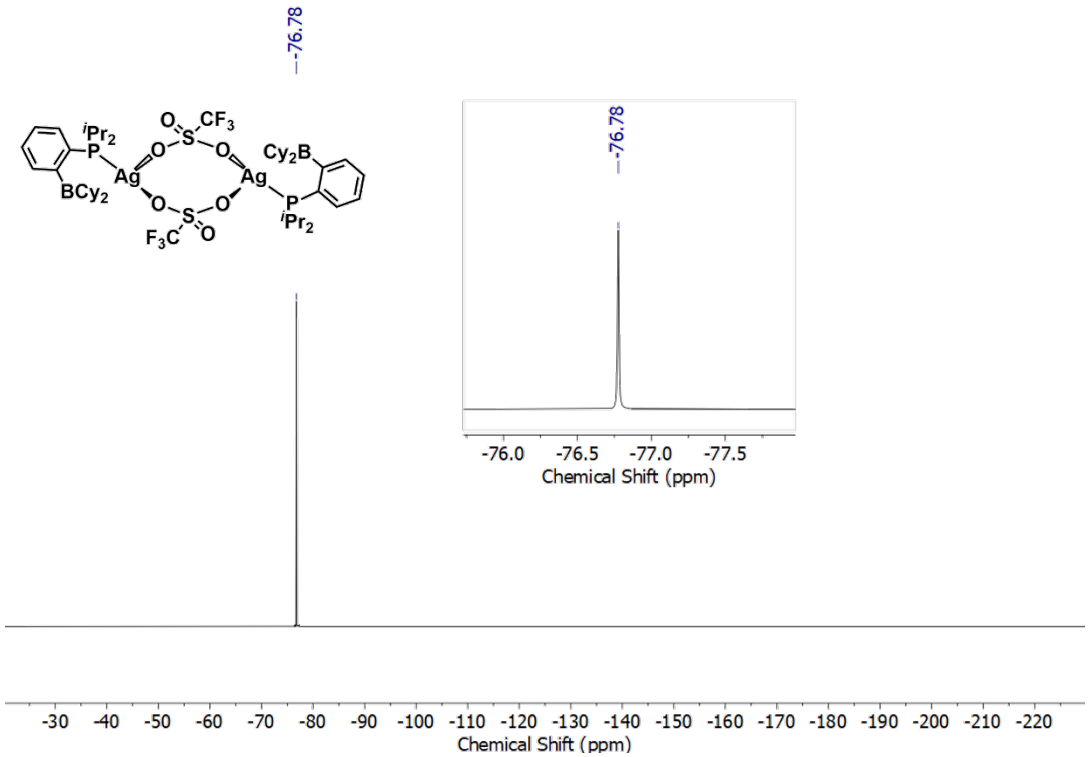

Figure S11. $^{19}F\{^{1}H\}$ NMR spectrum of $[PB\{AgOTf\}]_2$ in C_6D_6.

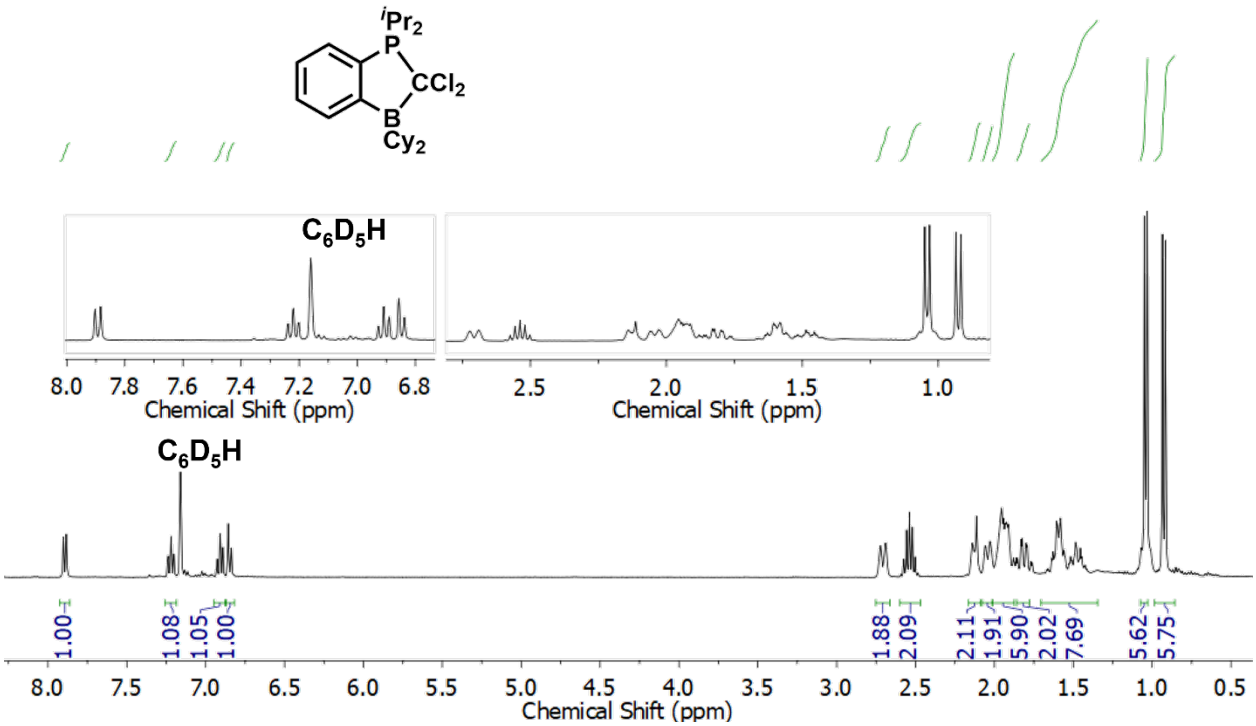

Figure S12. $^{1}H\{^{31}P\}$ NMR spectrum of $[PB\{CCl_2\}]$ (**6**) in C_6D_6.

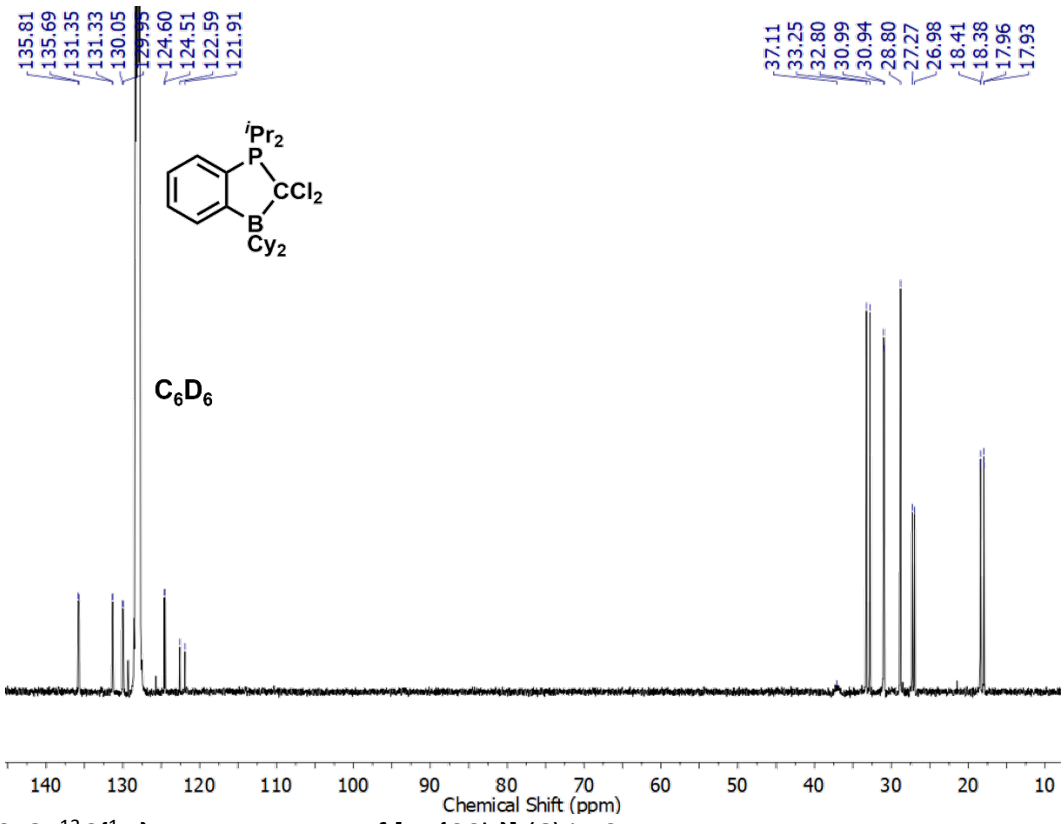

Figure S13. $^{13}C\{^{1}H\}$ NMR spectrum of [PB{CCl_2}] (**6**) in C_6D_6.

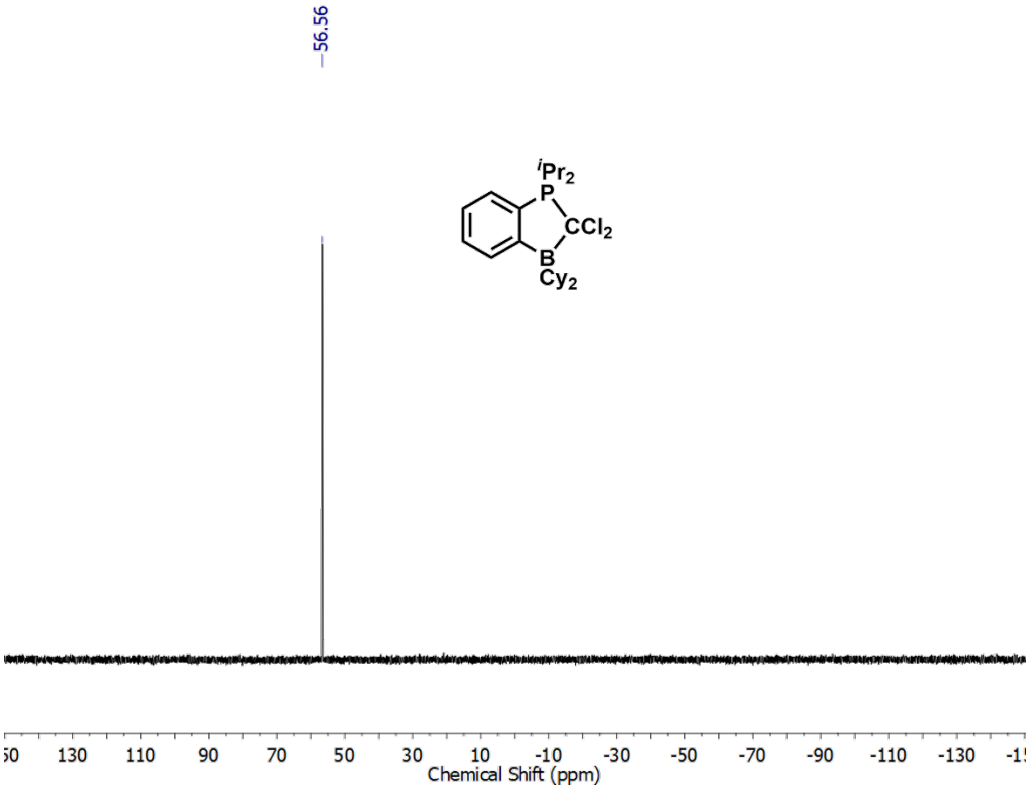

Figure S14. $^{31}P\{^{1}H\}$ NMR spectrum of [PB{CCl_2}] (**6**) in C_6D_6.

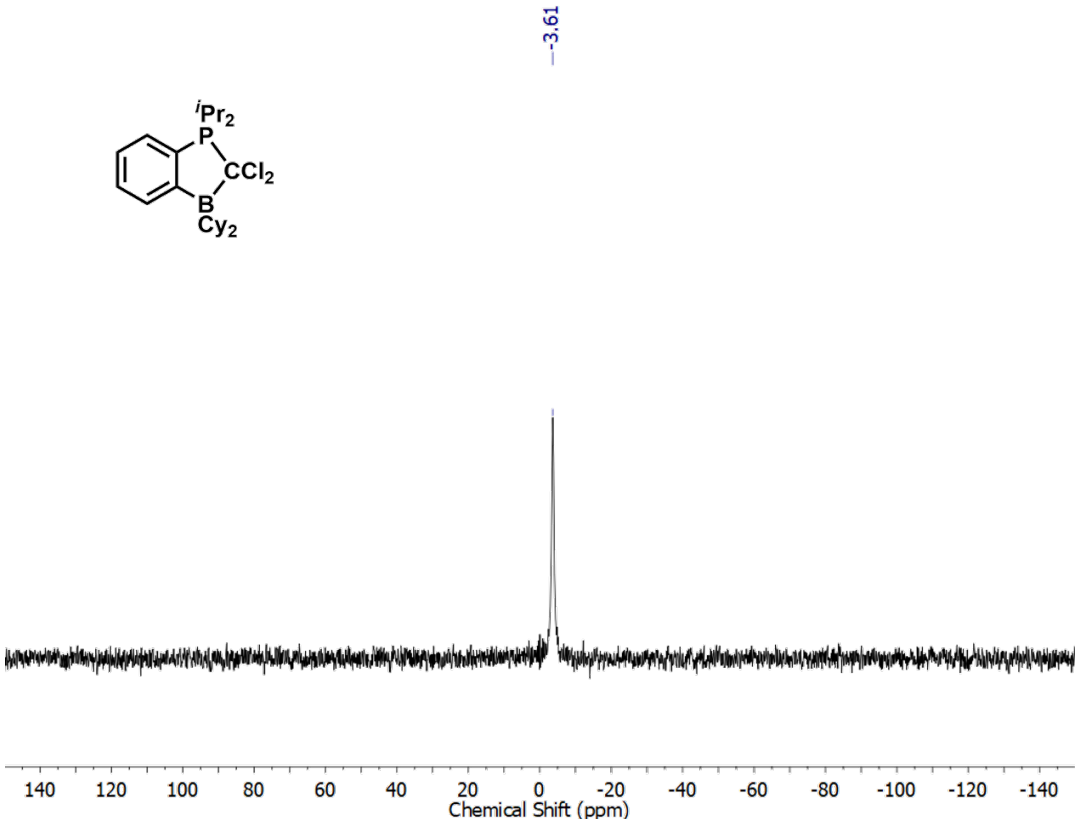

Figure S15. $^{11}B\{^{1}H\}$ NMR spectrum of [PB{CCl_2}] (**6**) in C_6D_6.

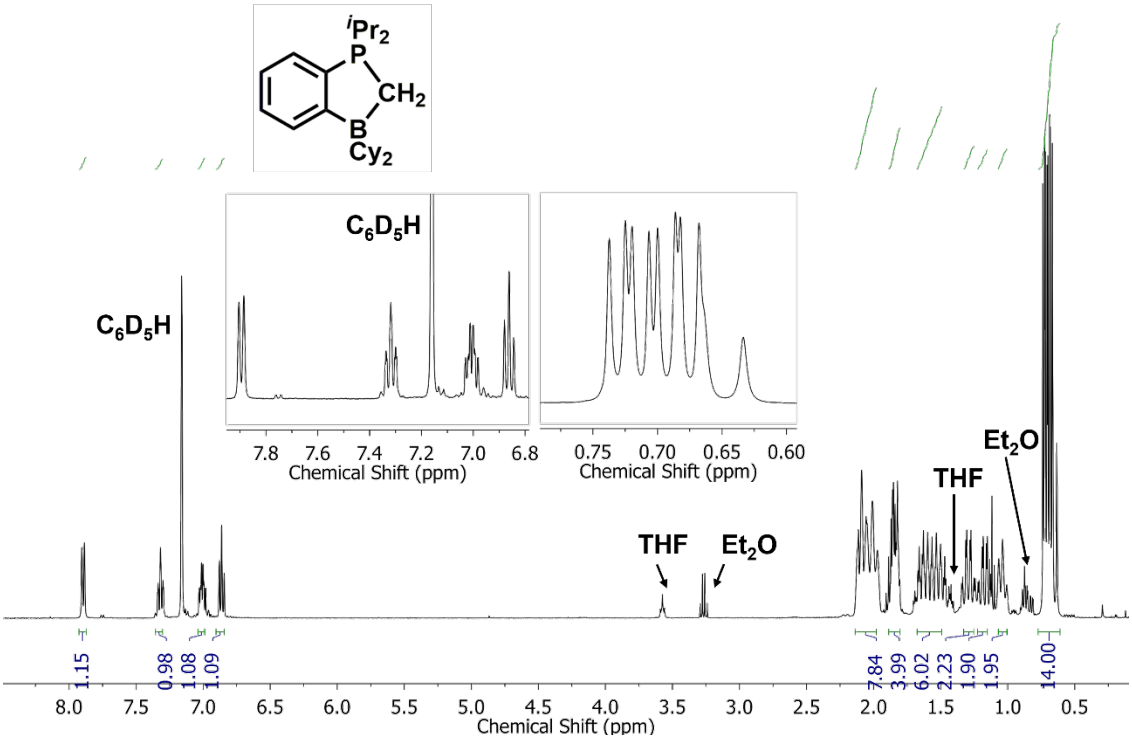

Figure S16. ^{1}H NMR spectrum of [PB{CH_2}] (**7**) in C_6D_6.

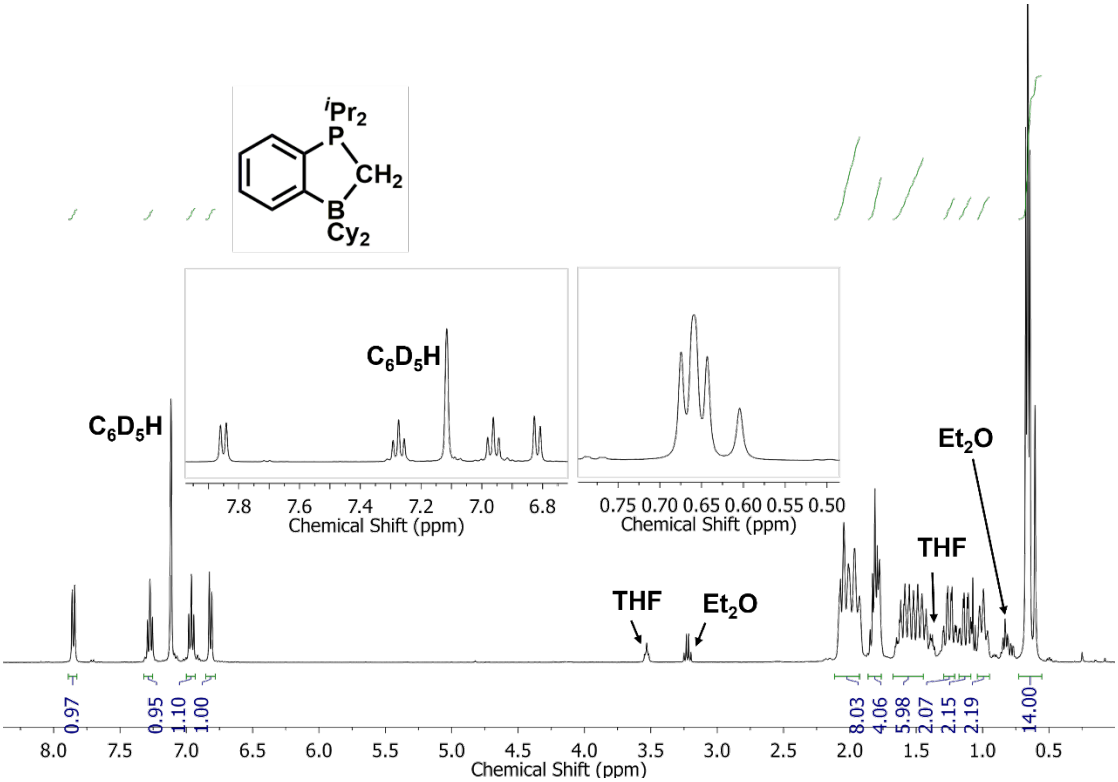

Figure S17. $^{1}H\{^{31}P\}$ NMR spectrum of [PB{CH_2}] (**7**) in C_6D_6.

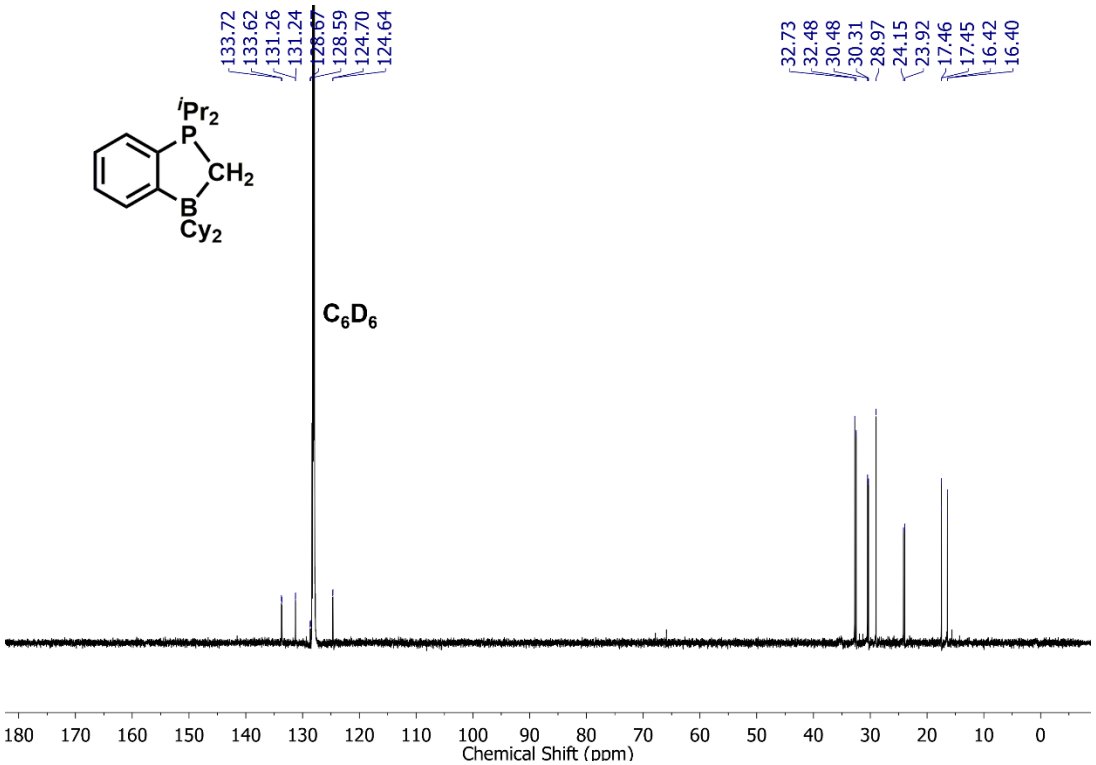

Figure S18. $^{13}C\{^{1}H\}$ NMR spectrum of [PB{CH_2}] (**7**) in C_6D_6.

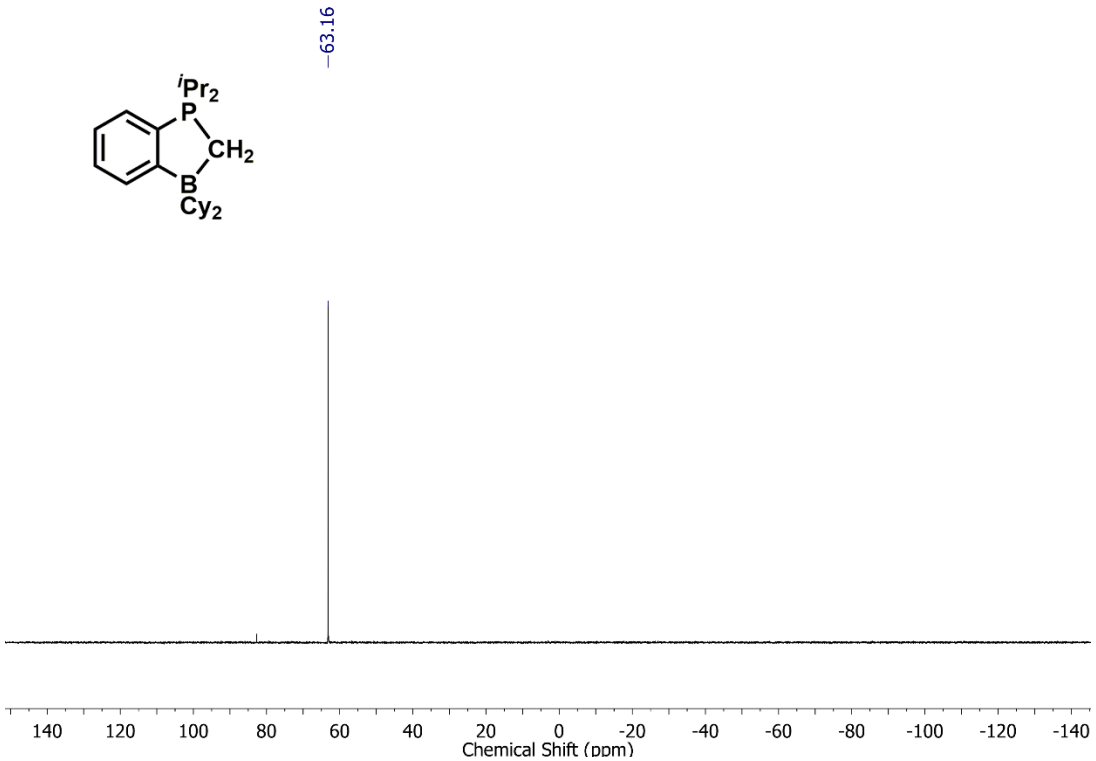

Figure S19. $^{31}P\{^{1}H\}$ NMR spectrum of [PB{CH_2}] (**7**) in C_6D_6.

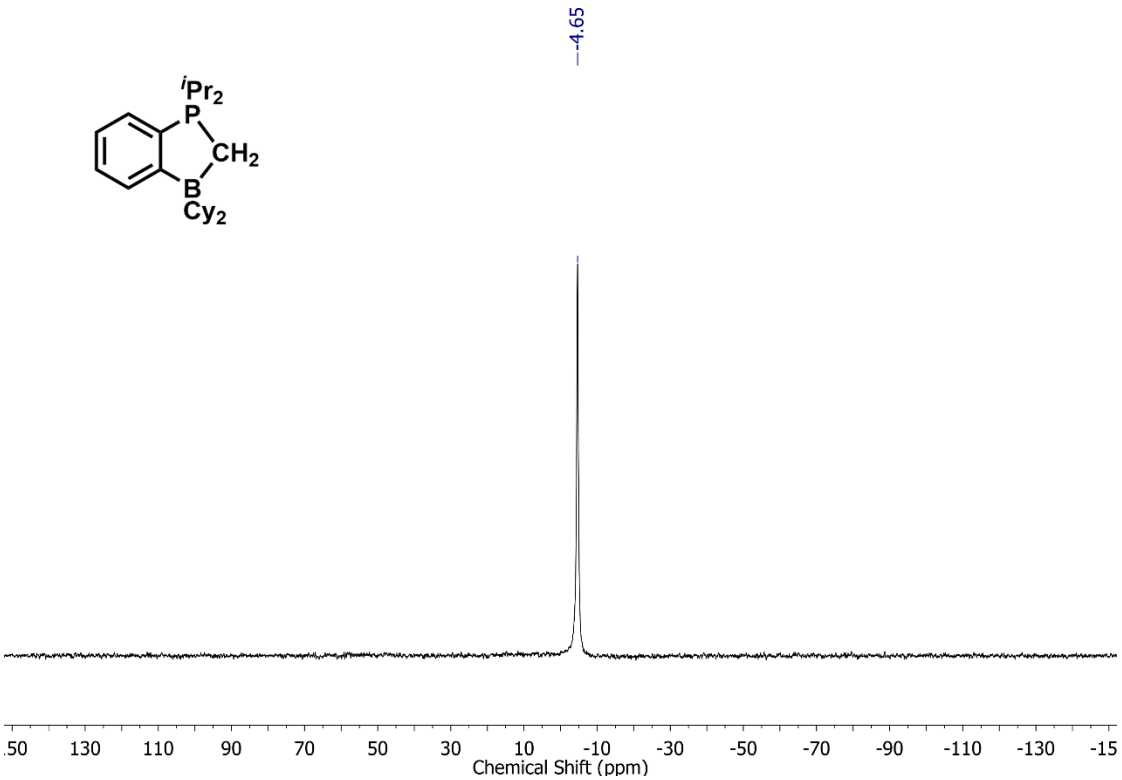

Figure S20. $^{11}B\{^{1}H\}$ NMR spectrum of [PB{CH_2}] (**7**) in C_6D_6.

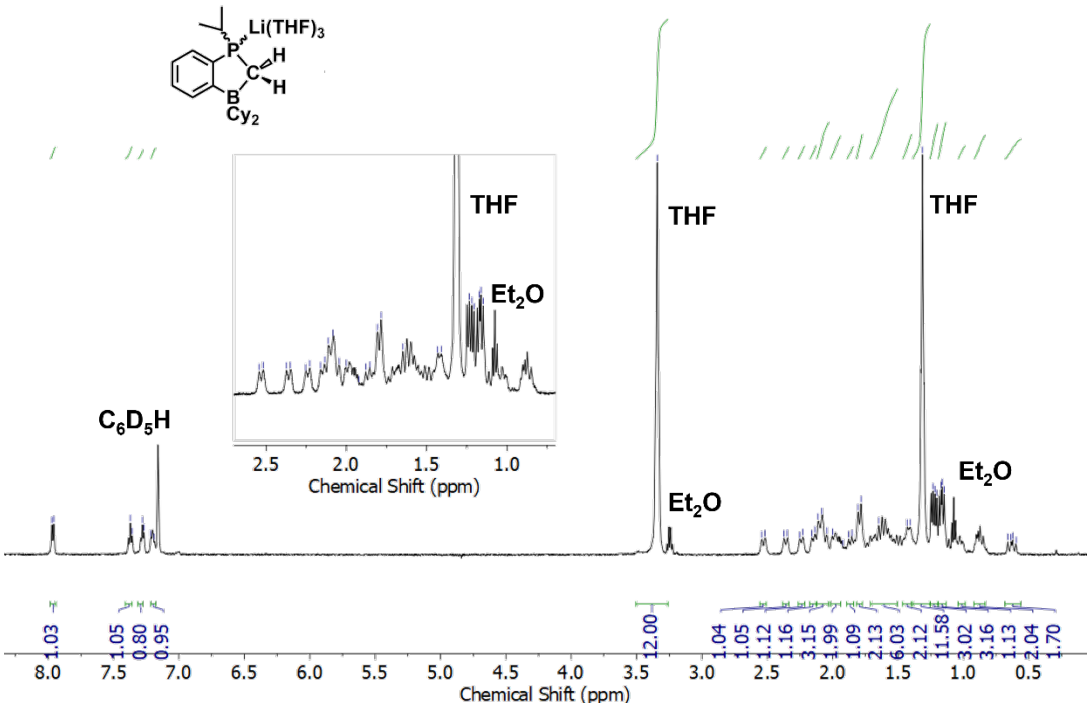

Figure S21. ^{1}H NMR spectrum of [{$(THF)_3Li^{i}PrP(C_6H_4)BCy_2\{CH_2\}$] (**8**) in C_6D_6.

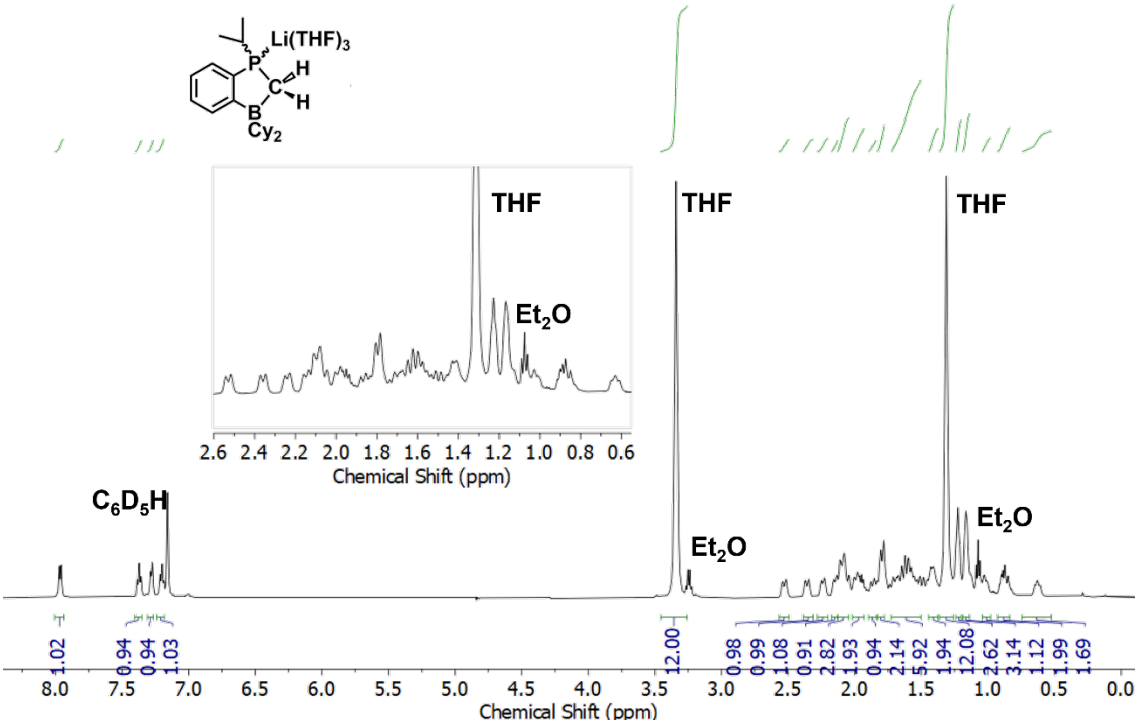

Figure S22. $^{1}H\{^{31}P\}$ NMR spectrum of [{$(THF)_3Li^{i}PrP(C_6H_4)BCy_2\{CH_2\}$] (**8**) in C_6D_6.

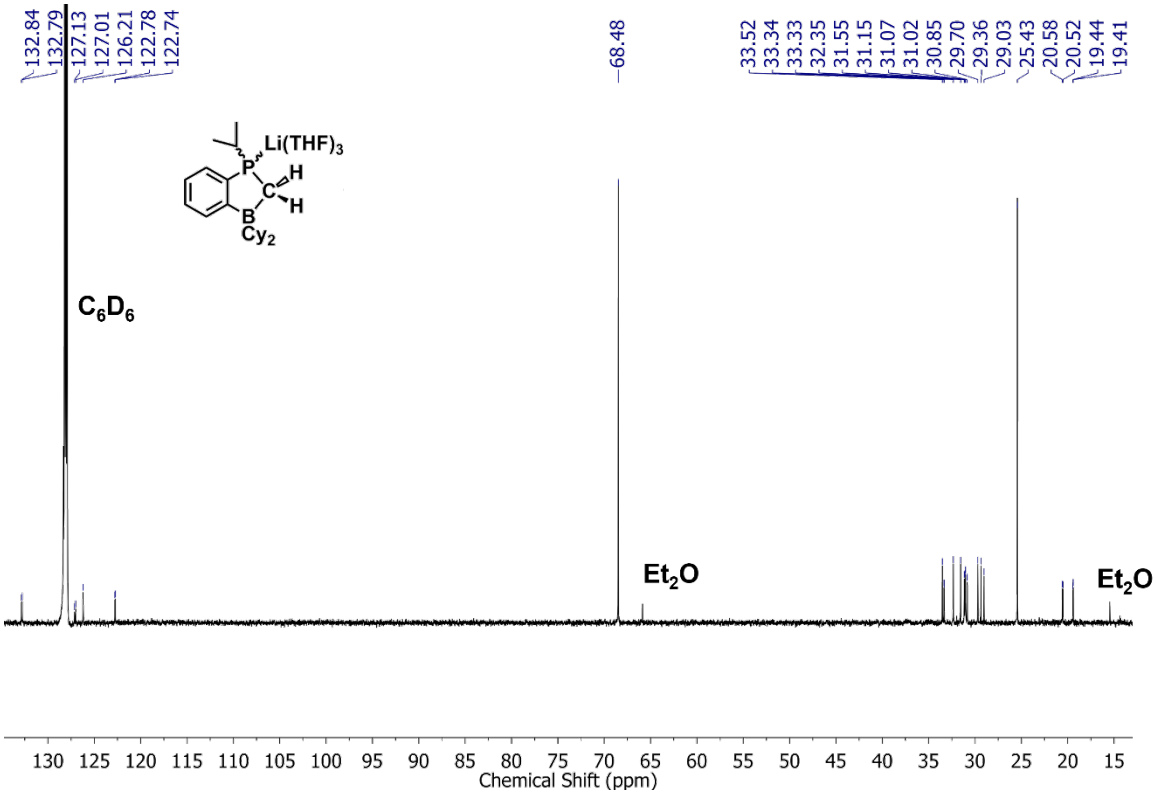

Figure S23. $^{13}C\{^{1}H\}$ NMR spectrum of [{(THF)$_3$Li}^{i}PrP(C$_6$H$_4$)BCy$_2${CH$_2$}] (**8**) in C$_6$D$_6$.

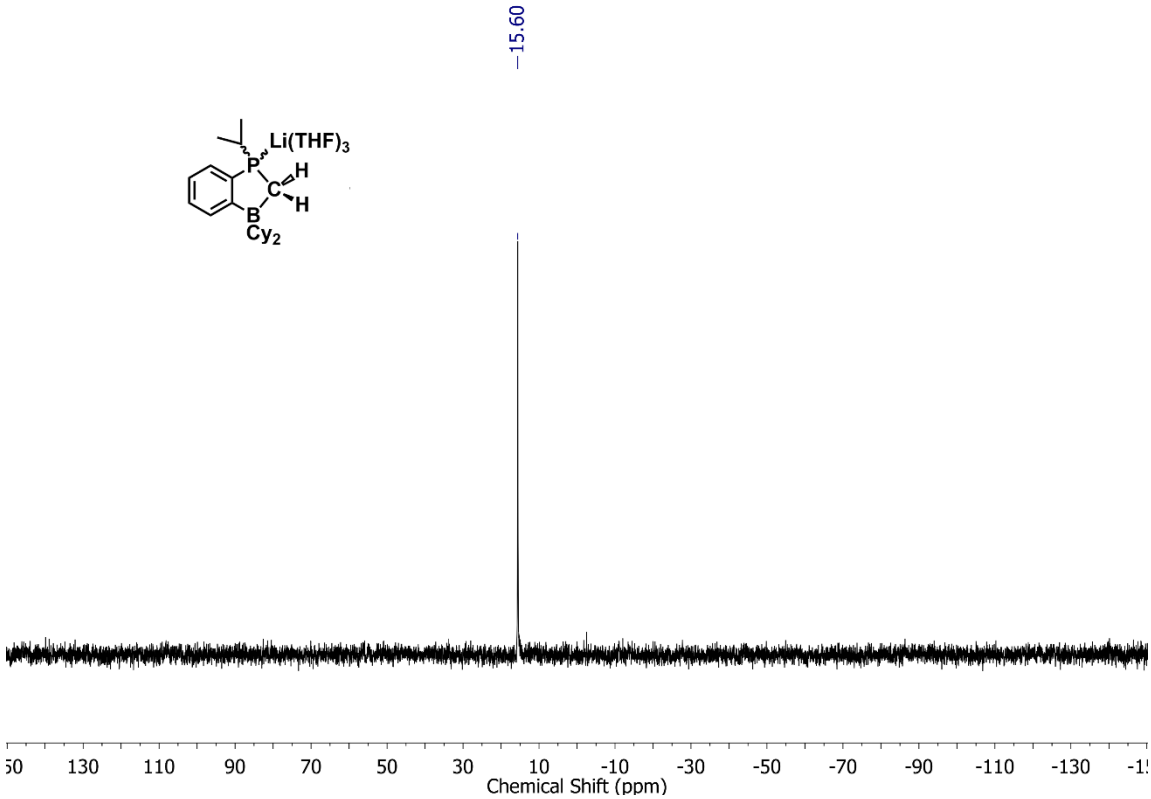

Figure S24. $^{31}P\{^{1}H\}$ NMR spectrum of [{(THF)$_3$Li}^{i}PrP(C$_6$H$_4$)BCy$_2${CH$_2$}] (**8**) in C$_6$D$_6$.

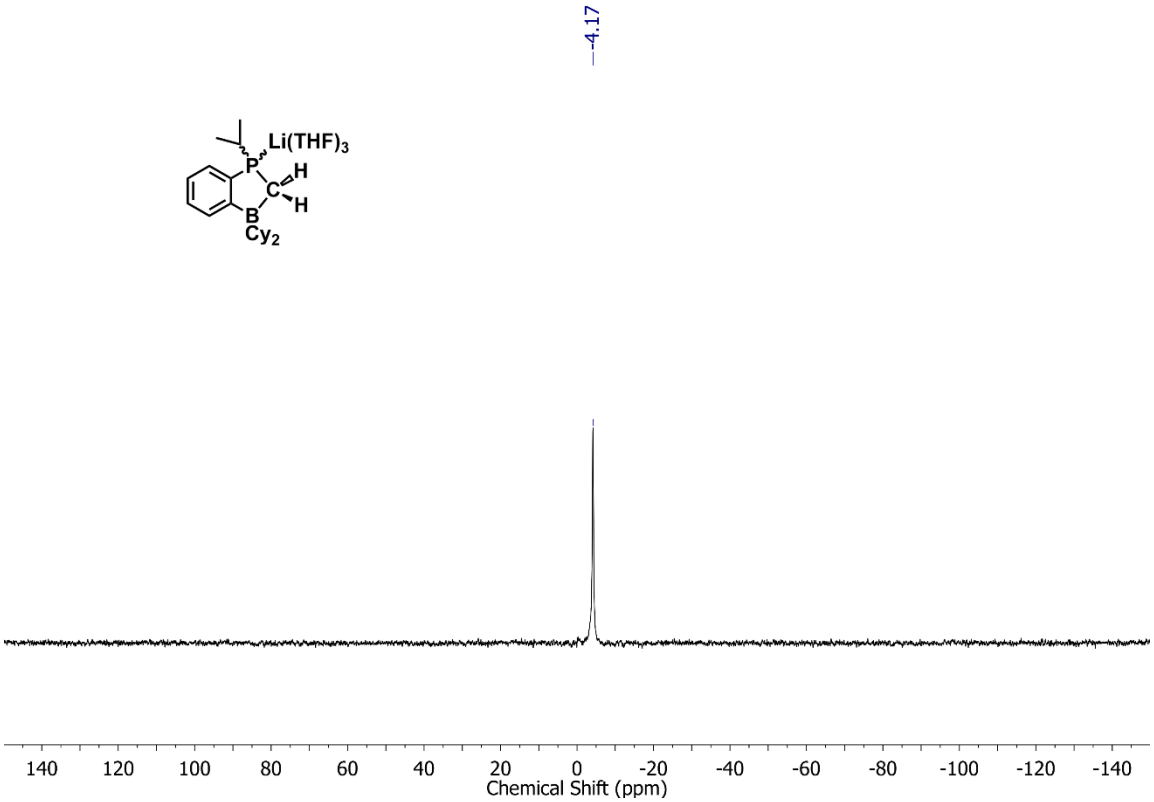

Figure S25. $^{11}B\{^{1}H\}$ NMR spectrum of [{$(THF)_3Li$}^{i}PrP$(C_6H_4)BCy_2\{CH_2\}$] (**8**) in C_6D_6.

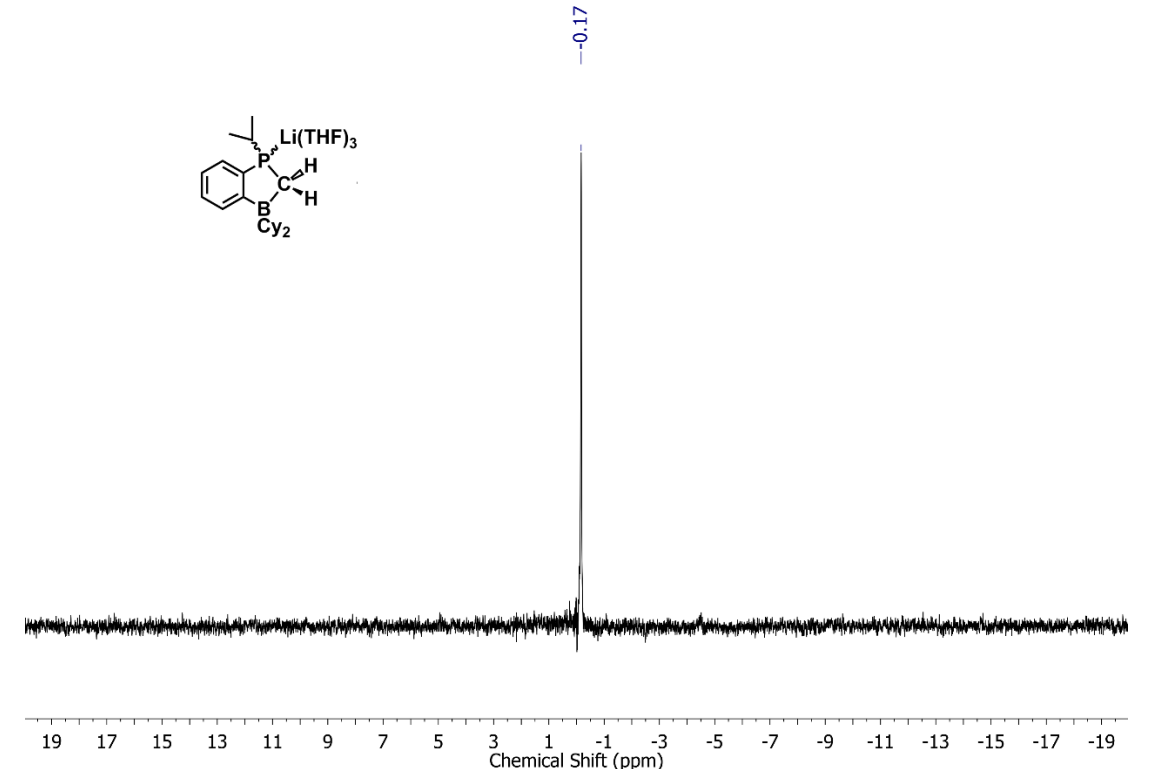

Figure S26. $^{7}Li\{^{1}H\}$ NMR spectrum of [{$(THF)_3Li$}^{i}PrP$(C_6H_4)BCy_2\{CH_2\}$] (**8**) in C_6D_6.

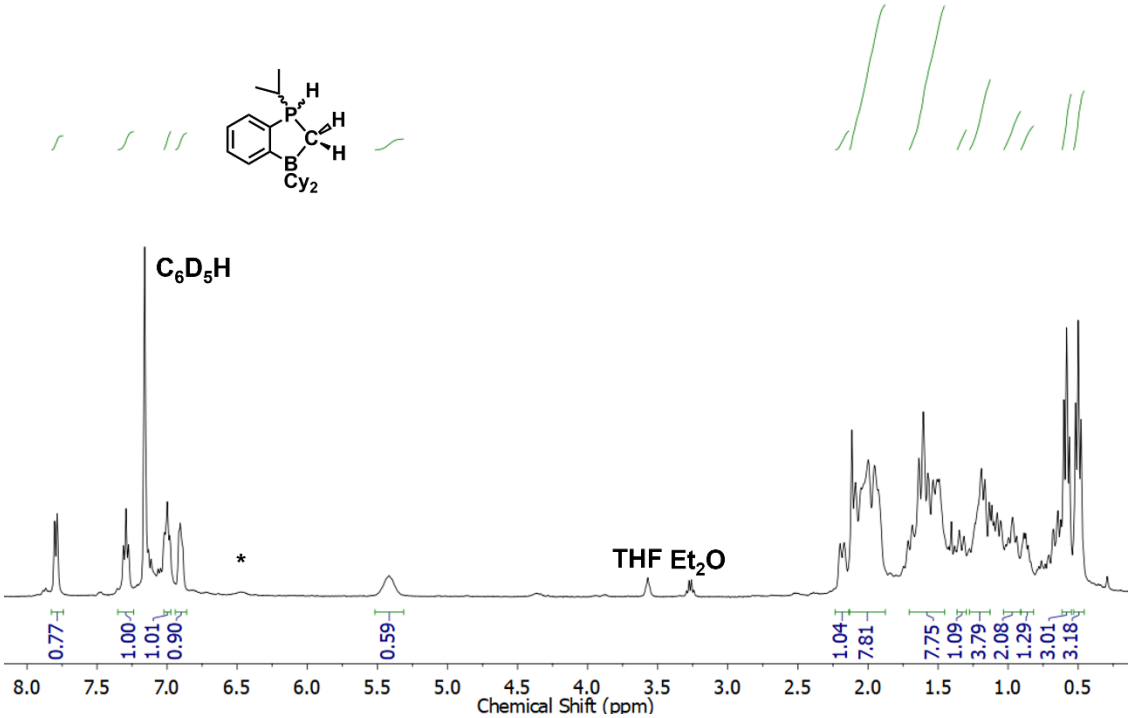

Figure S27. $^{1}H\{^{31}P\}$ NMR spectrum of [^{i}Pr(H)P(C_6H_4)BCy_2{CH_2}] (**9**) in C_6D_6. Peaks labelled with an asterisk (*) are unknown.

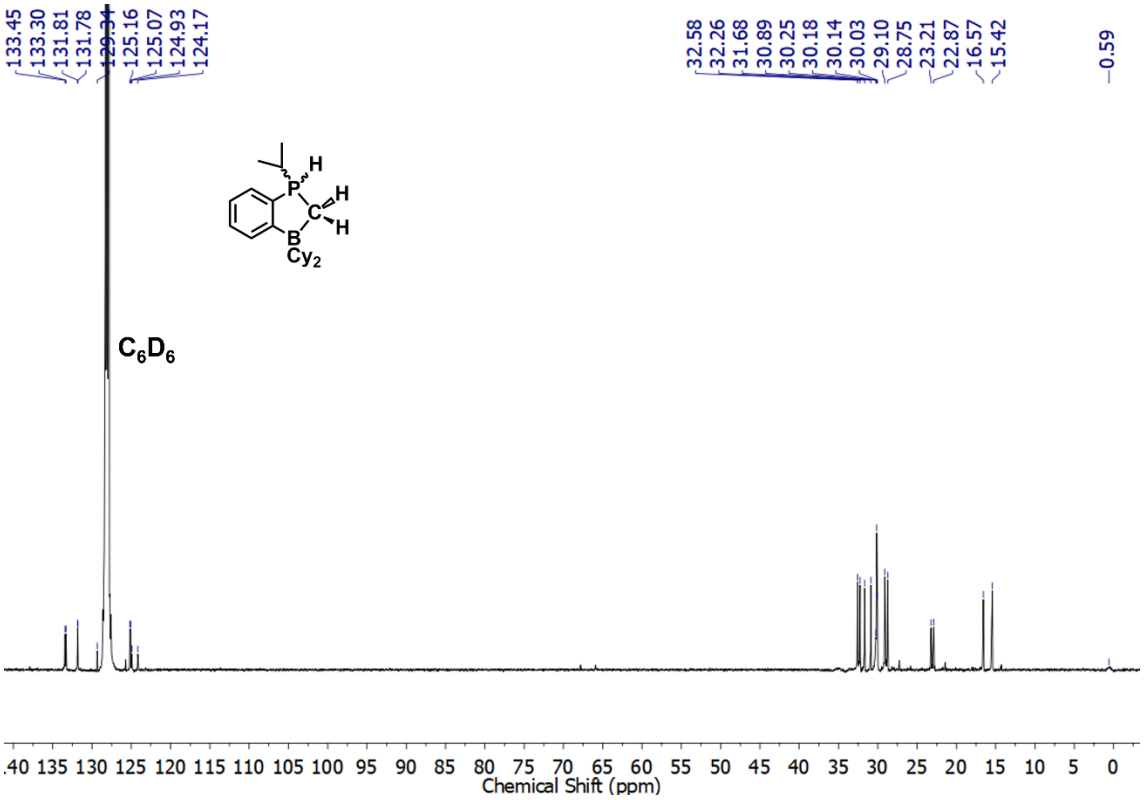

Figure S28. $^{13}C\{^{1}H\}$ NMR spectrum of [^{i}Pr(H)P(C_6H_4)BCy_2{CH_2}] (**9**) in C_6D_6.

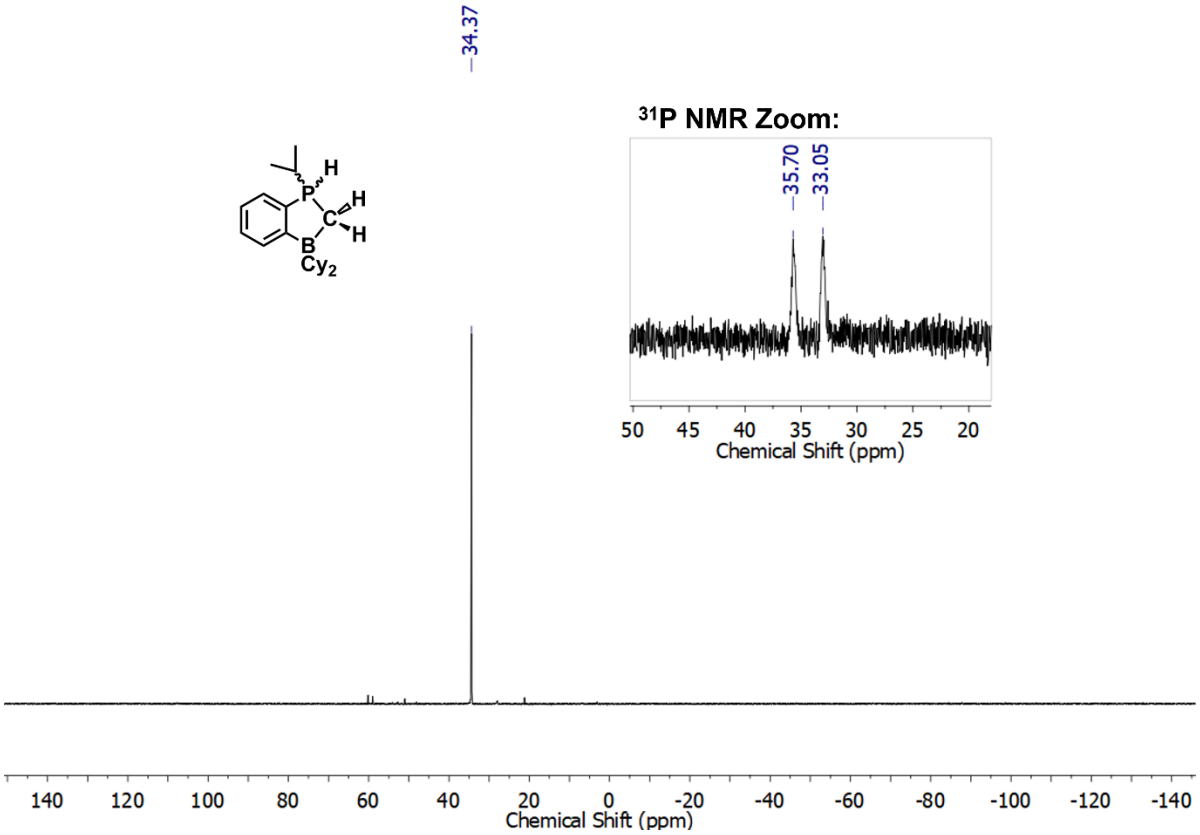

Figure S29. $^{31}P\{^{1}H\}$ NMR spectrum of [^{i}Pr(H)P(C_6H_4)BCy_2{CH_2}] (**9**) in C_6D_6.

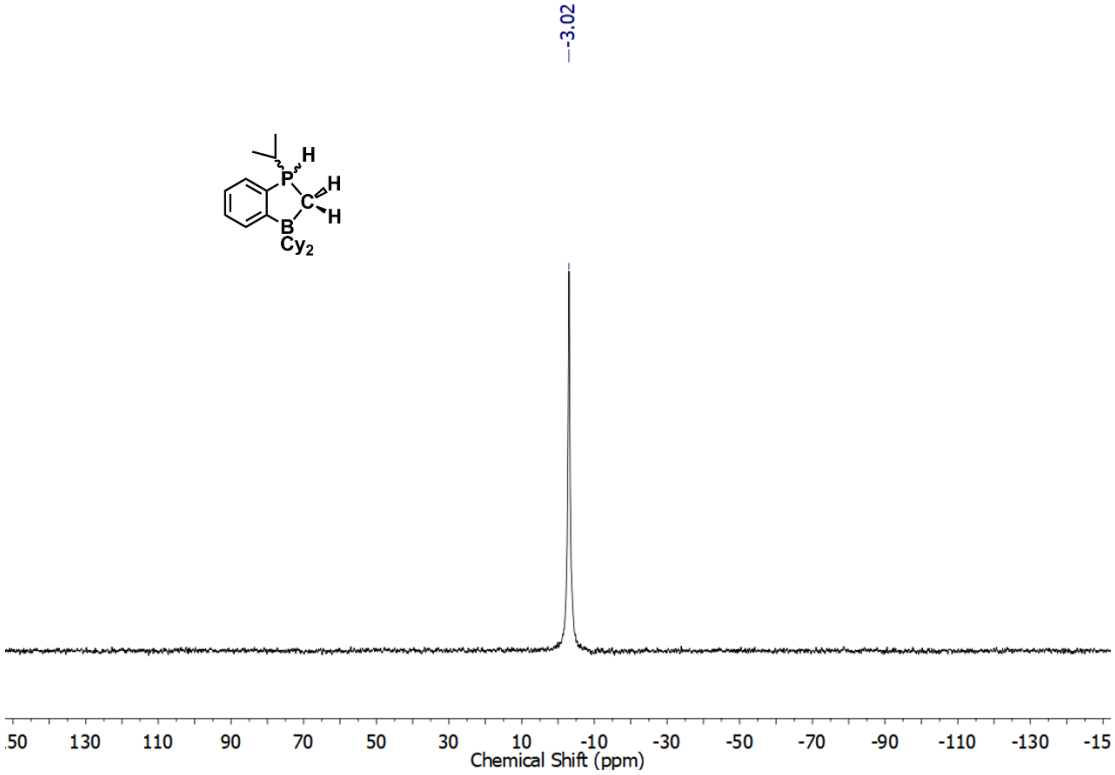

Figure S30. $^{11}B\{^{1}H\}$ NMR spectrum of [^{i}Pr(H)P(C_6H_4)BCy_2{CH_2}] (**9**) in C_6D_6.

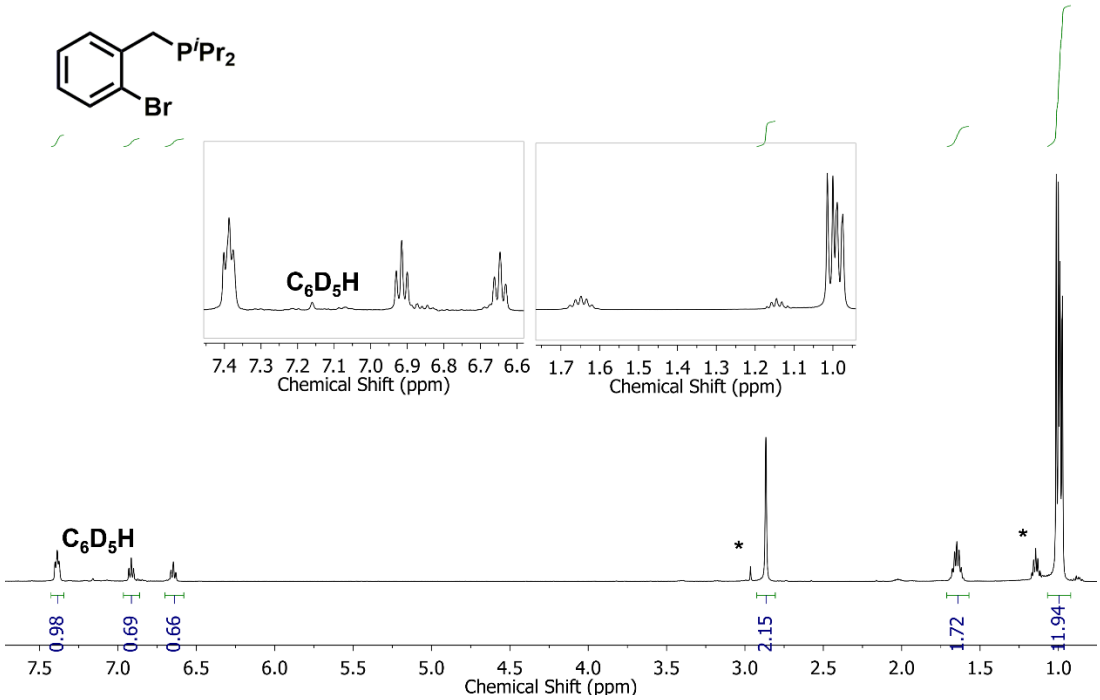

Figure S31. ^{1}H NMR spectrum of $^{i}Pr_2PCH_2(C_6H_4)Br$ in C_6D_6. Peaks labelled with an asterisk (*) are unknown; however, it is likely $(^{i}Pr_2P)_2$ since the ^{31}P NMR of this sample (Figure S34; see below) shows an impurity consistent with the reported ^{31}P data for $(^{i}Pr_2P)_2$.[S6]

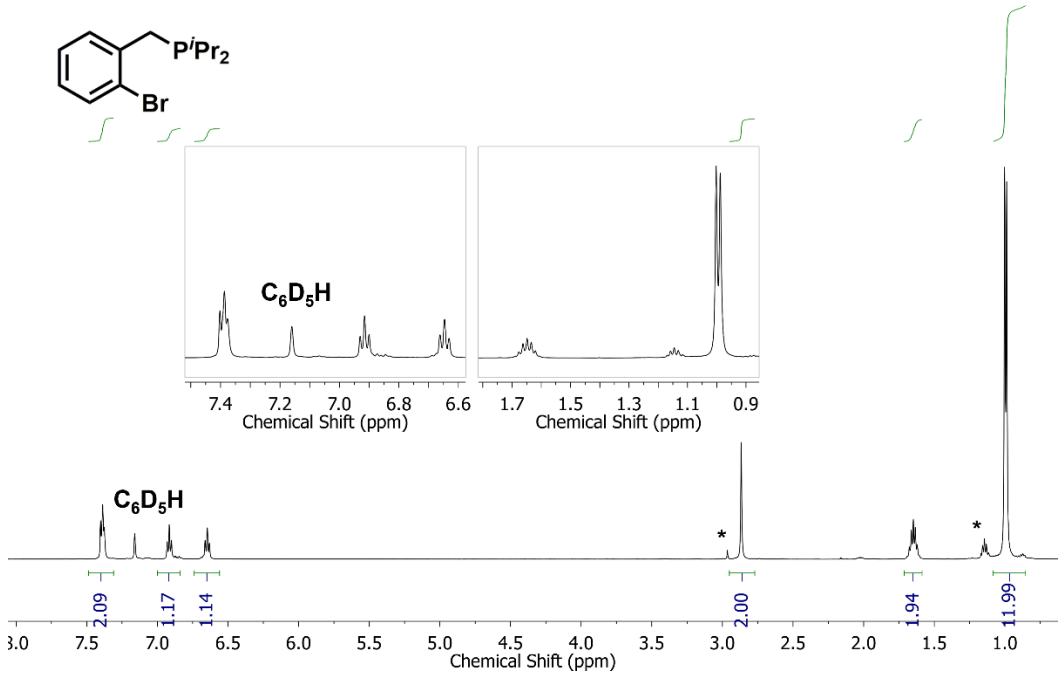

Figure S32. $^{1}H\{^{31}P\}$ NMR spectrum of $^{i}Pr_2PCH_2(C_6H_4)Br$ in C_6D_6. Peaks labelled with an asterisk (*) are unknown; however, it is likely $(^{i}Pr_2P)_2$ since the ^{31}P NMR of this sample (Figure S34; see below) shows an impurity consistent with the reported ^{31}P data for $(^{i}Pr_2P)_2$.[S6]

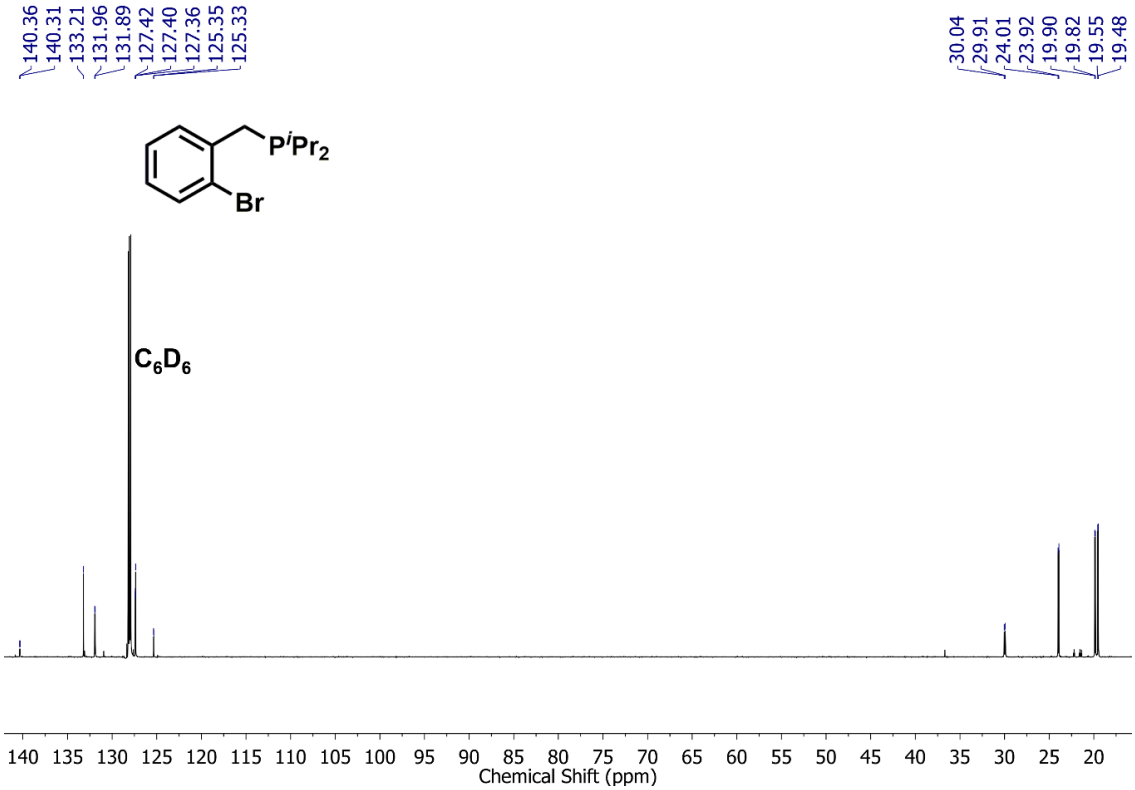

Figure S33. $^{13}C\{^1H\}$ NMR spectrum of $^iPr_2PCH_2(C_6H_4)Br$ in C_6D_6.

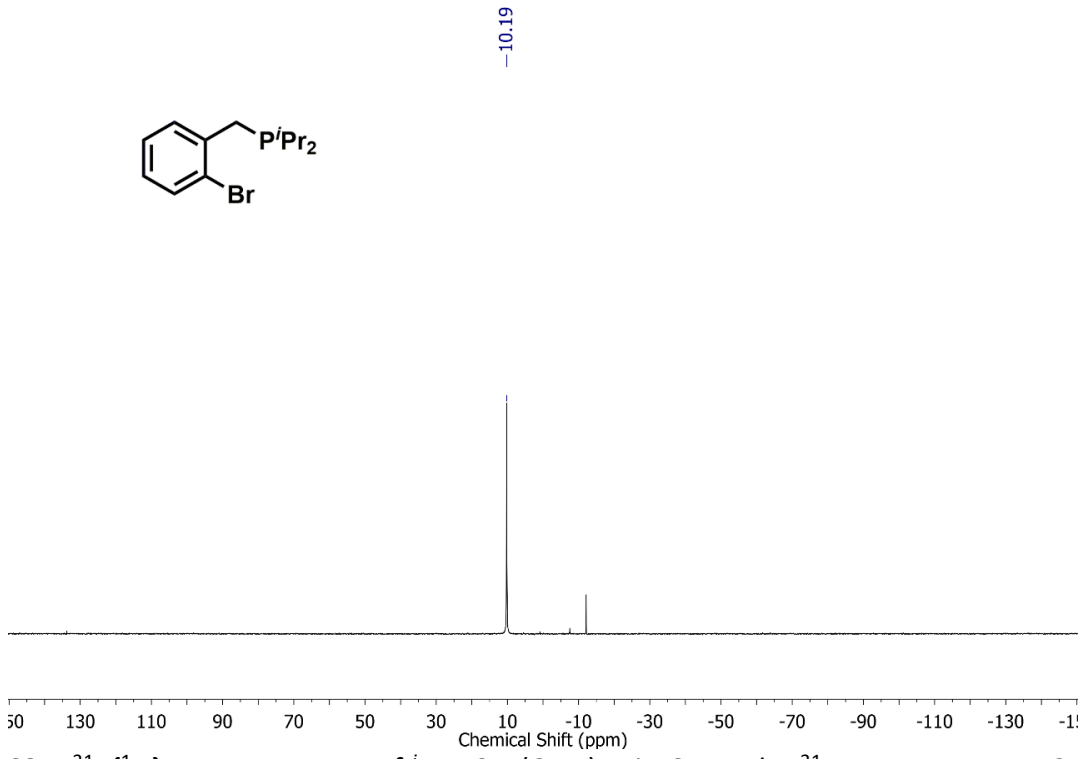

Figure S34. $^{31}P\{^1H\}$ NMR spectrum of $^iPr_2PCH_2(C_6H_4)Br$ in C_6D_6. The ^{31}P resonance at -12 ppm is consisted with the reported ^{31}P data for $(^iPr_2P)_2$.[S6]

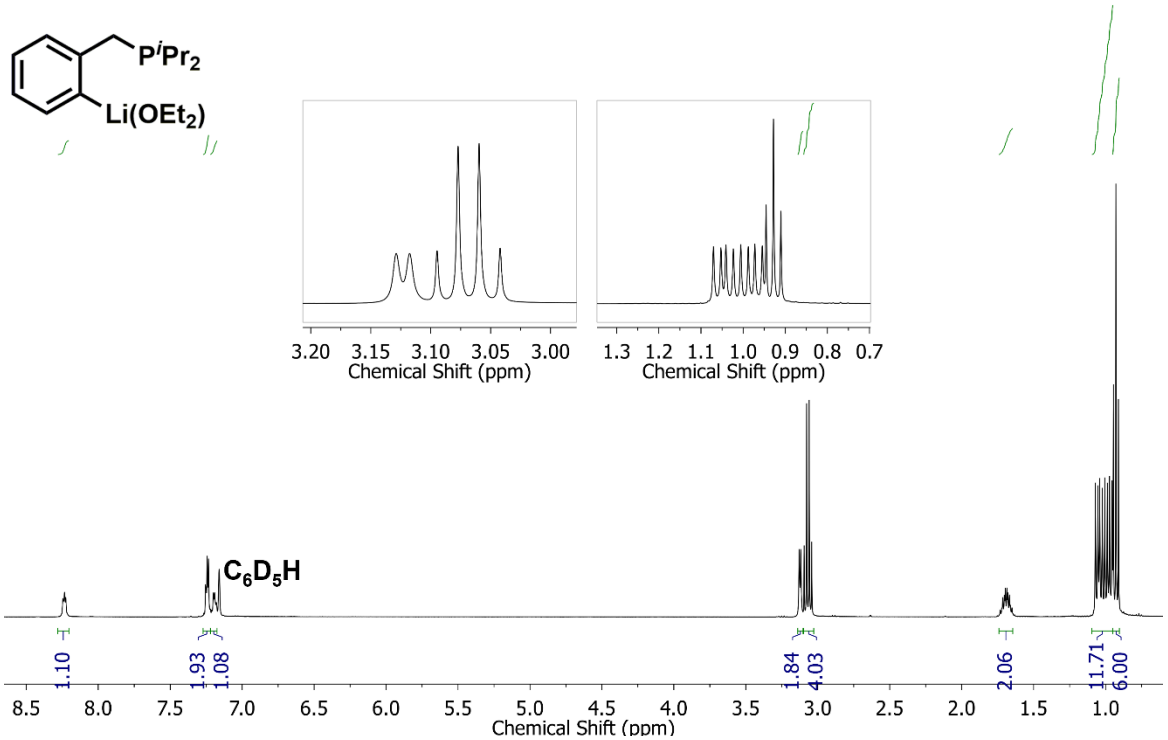

Figure S35. ^{1}H NMR spectrum of [^{i}Pr$_2$PCH$_2$(C$_6$H$_4$)Li(OEt$_2$)]$_2$ (**10**) in C$_6$D$_6$.

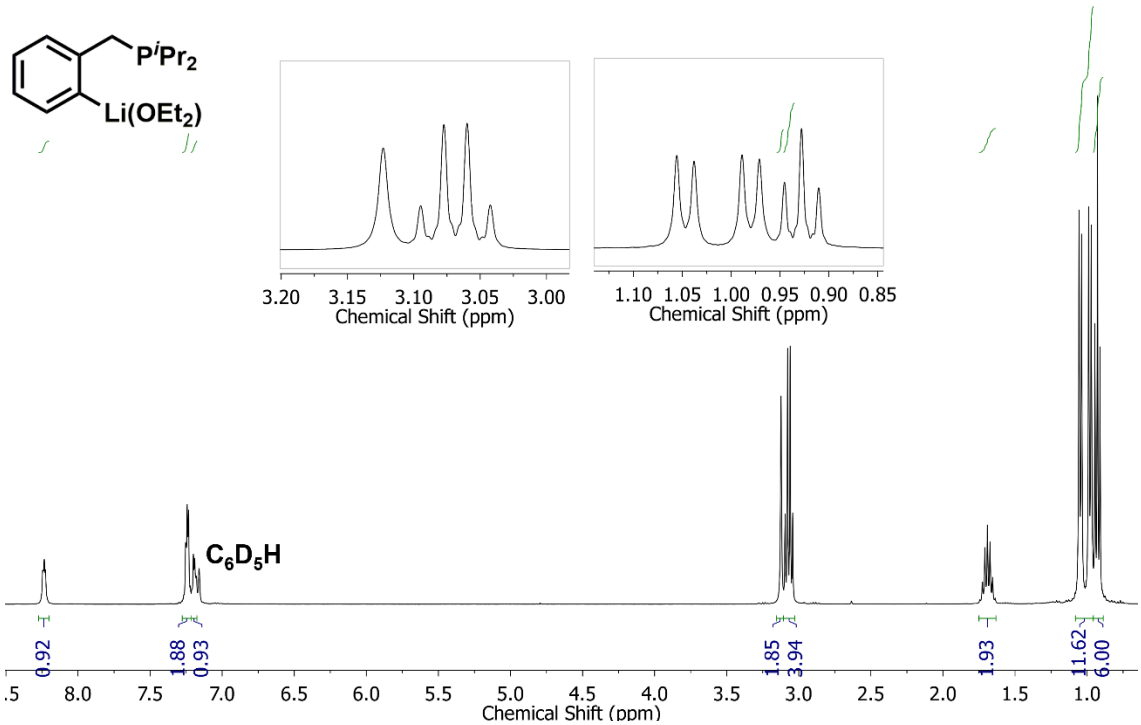

Figure S36. ^{1}H{^{31}P} NMR spectrum of [^{i}Pr$_2$PCH$_2$(C$_6$H$_4$)Li(OEt$_2$)]$_2$ (**10**) in C$_6$D$_6$.

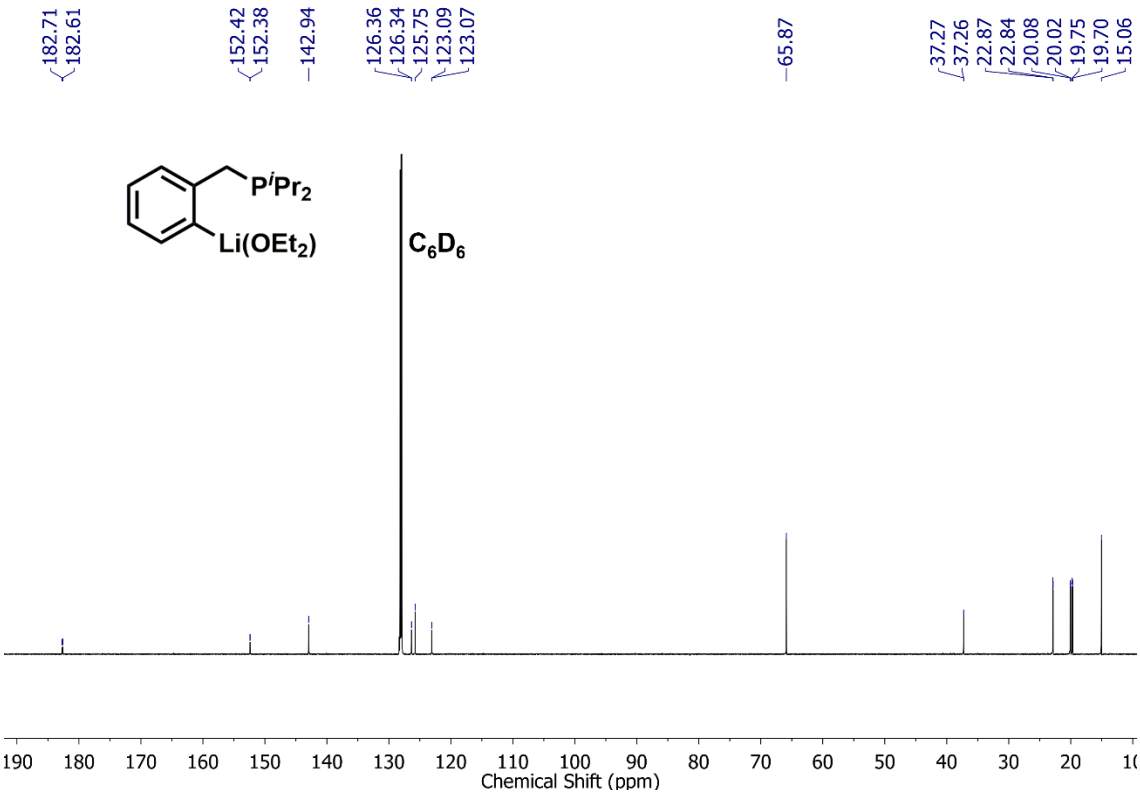

Figure S37. $^{13}C\{^1H\}$ NMR spectrum of $[^iPr_2PCH_2(C_6H_4)Li(OEt_2)]_2$ (**10**) in C_6D_6.

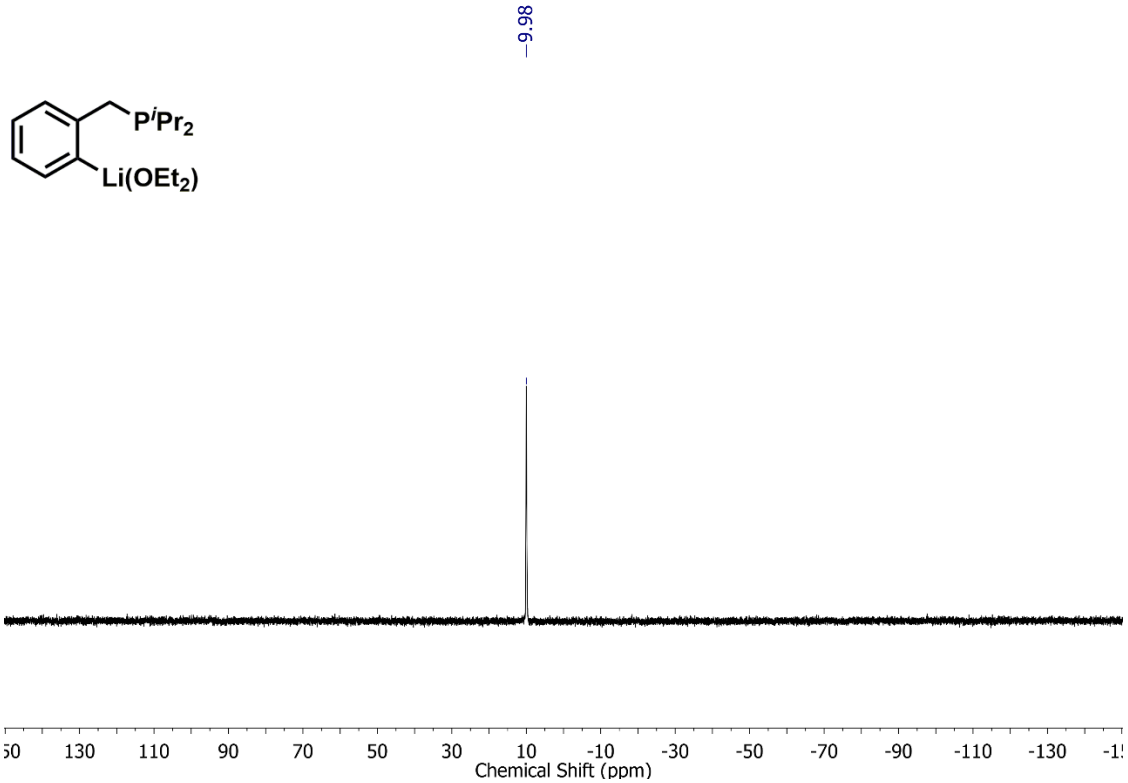

Figure S38. $^{31}P\{^1H\}$ NMR spectrum of $[^iPr_2PCH_2(C_6H_4)Li(OEt_2)]_2$ (**10**) in C_6D_6.

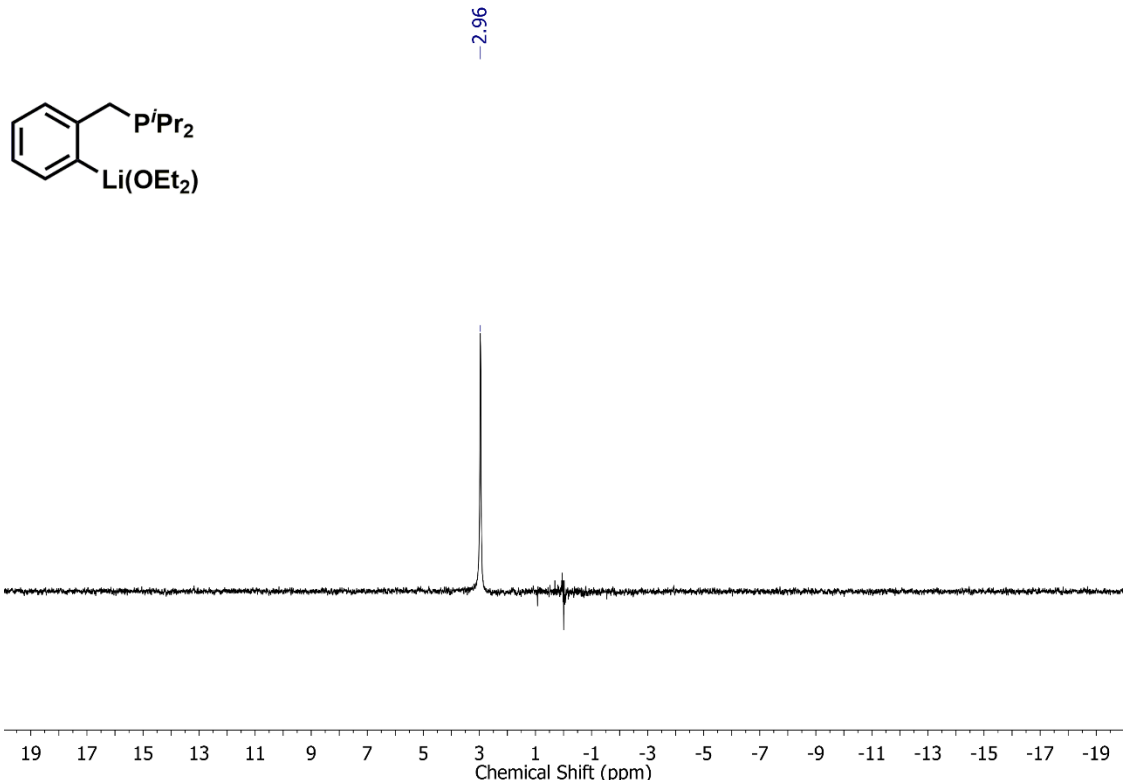

Figure S39. ^{7}Li{^{1}H} NMR spectrum of [^{i}Pr$_2$PCH$_2$(C$_6$H$_4$)Li(OEt$_2$)]$_2$ (**10**) in C$_6$D$_6$.

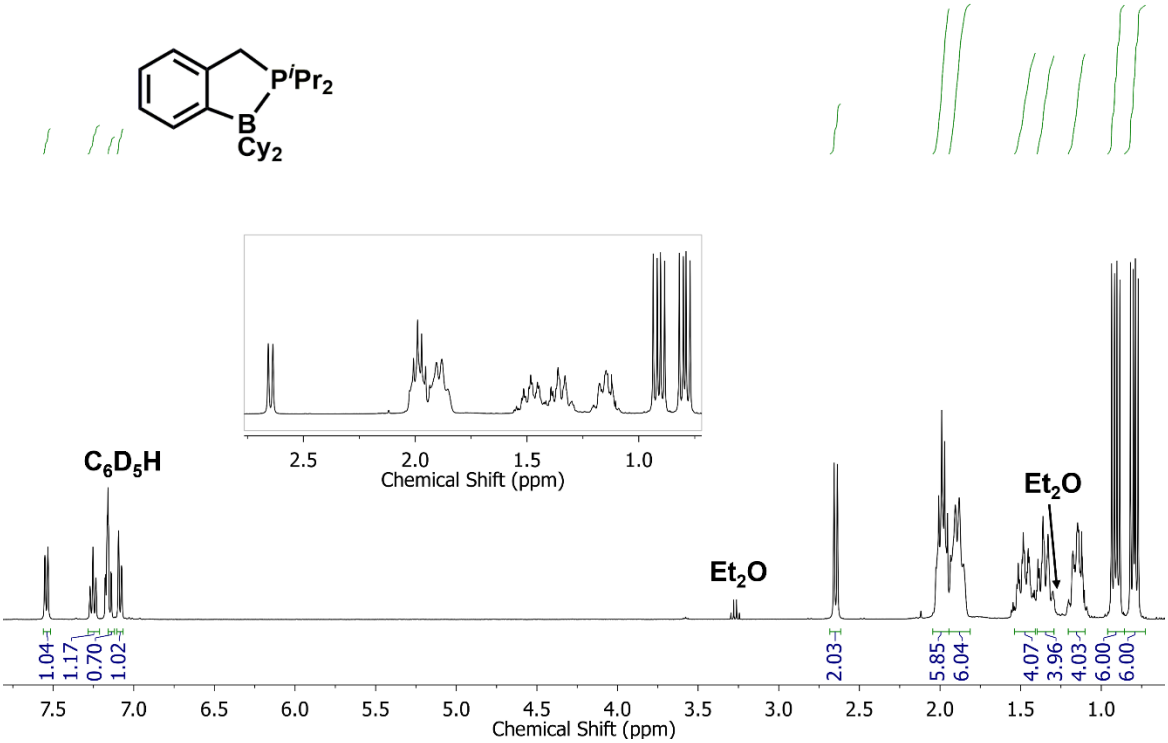

Figure S40. ^{1}H NMR spectrum of ^{i}Pr$_2$PCH$_2$(C$_6$H$_4$)BCy$_2$ (**^{CH2}PB**) in C$_6$D$_6$.

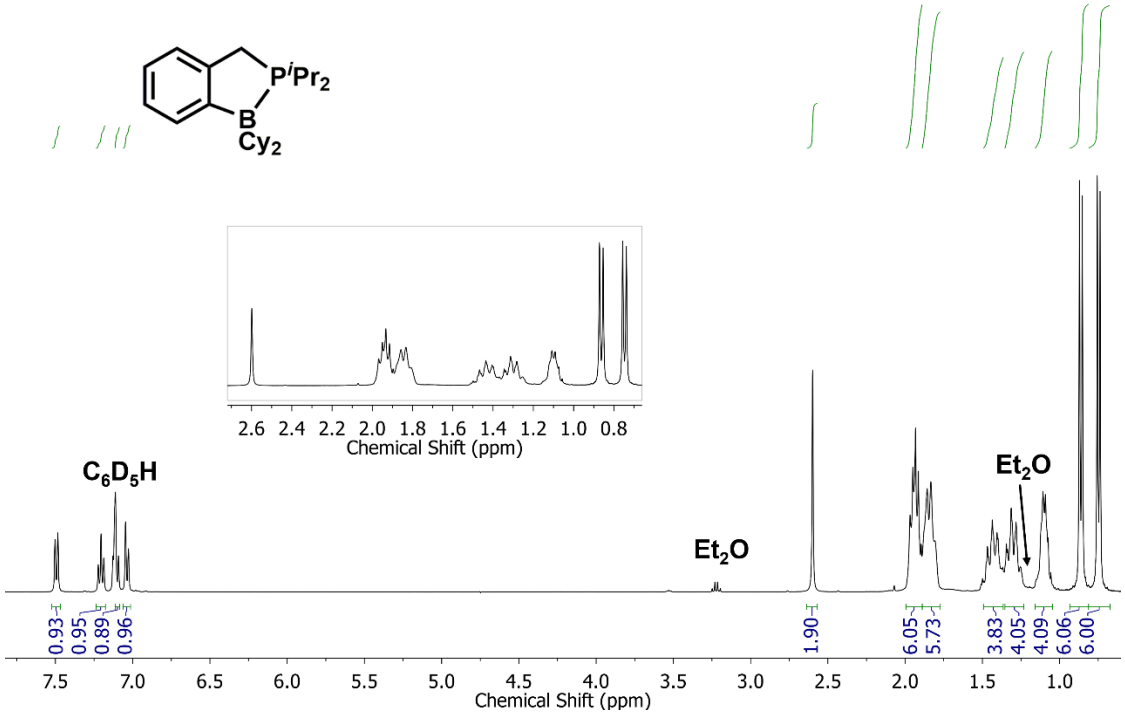

Figure S41. $^{1}H\{^{31}P\}$ NMR spectrum of $^{i}Pr_2PCH_2(C_6H_4)BCy_2$ (**^{CH2}PB**) in C_6D_6.

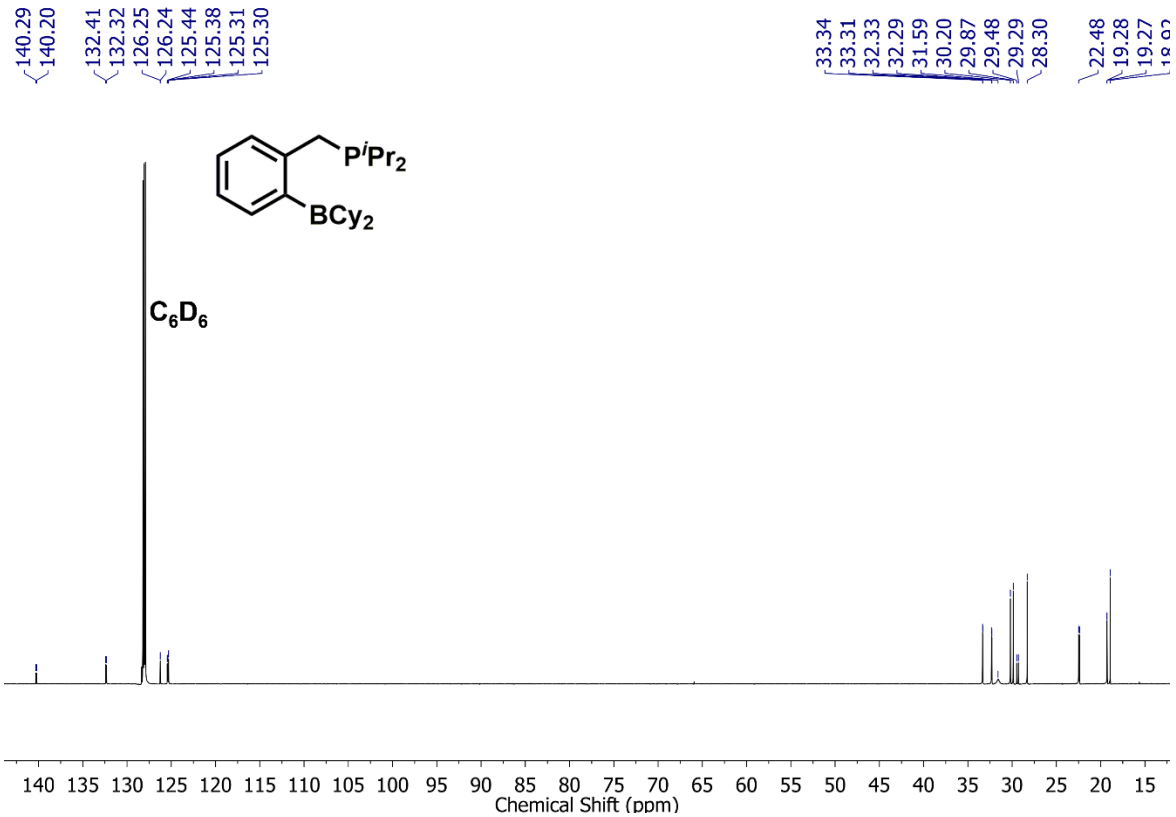

Figure S42. $^{13}C\{^{1}H\}$ NMR spectrum of $^{i}Pr_2PCH_2(C_6H_4)BCy_2$ (**^{CH2}PB**) in C_6D_6.

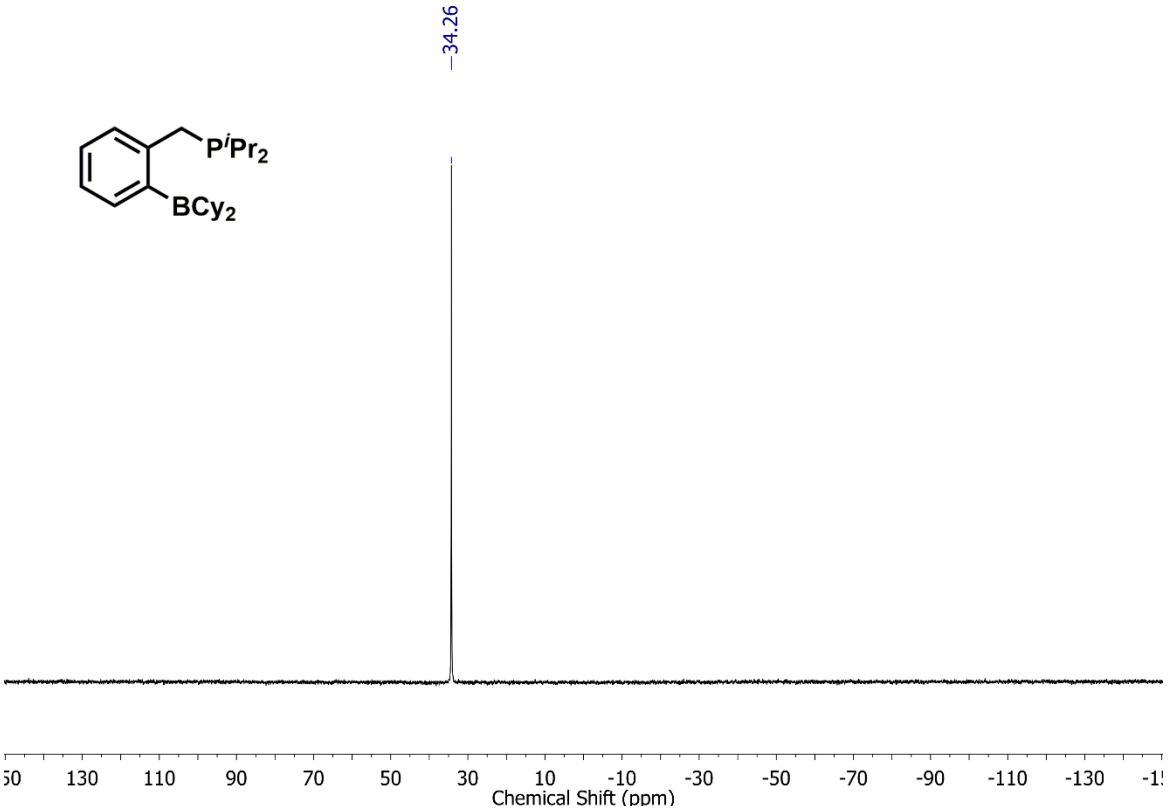

Figure S43. $^{31}P\{^1H\}$ NMR spectrum of ^{i}Pr$_2$PCH$_2$(C$_6$H$_4$)BCy$_2$ (**^{CH2}PB**) in C$_6$D$_6$.

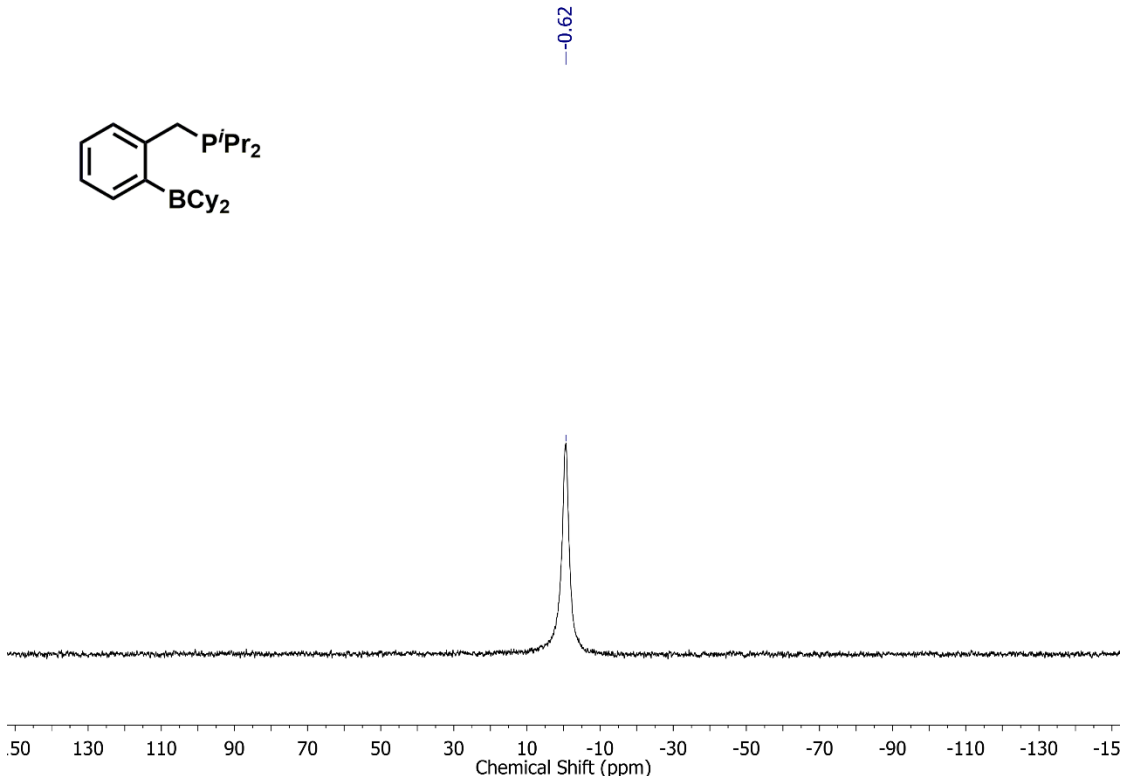

Figure S44. $^{11}B\{^1H\}$ NMR spectrum of ^{i}Pr$_2$PCH$_2$(C$_6$H$_4$)BCy$_2$ (**^{CH2}PB**) in C$_6$D$_6$.

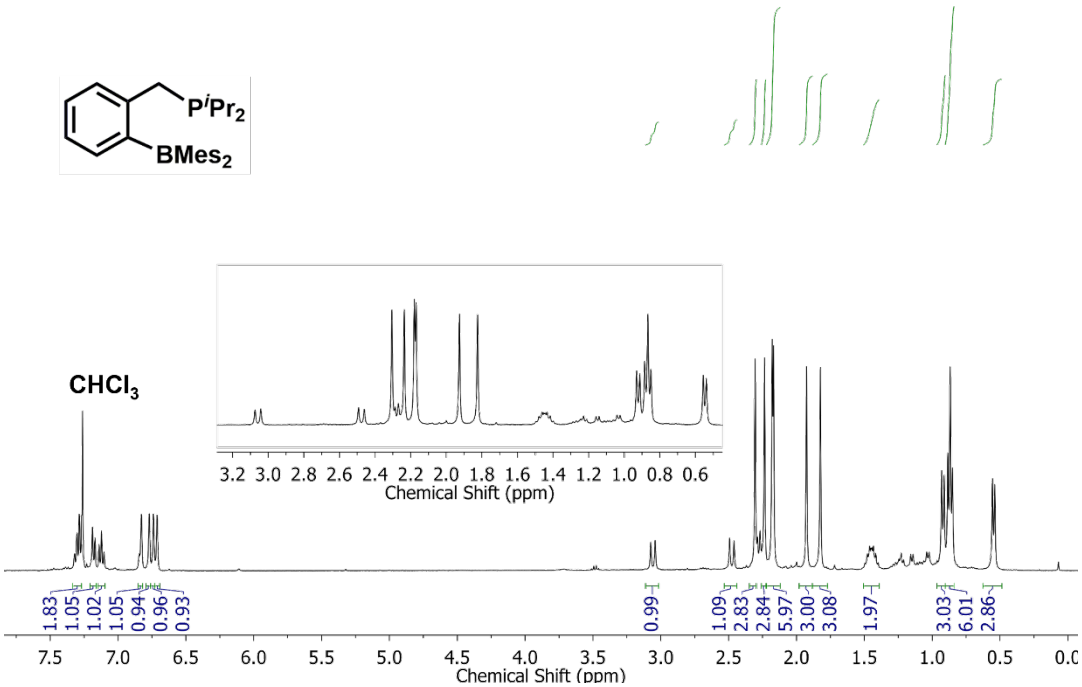

Figure S45. $^{1}H\{^{31}P\}$ NMR spectrum of $^{i}Pr_2PCH_2(C_6H_4)BMes_2$ ($^{CH2}PB_{Mes}$) in $CDCl_3$ collected at -40 °C.

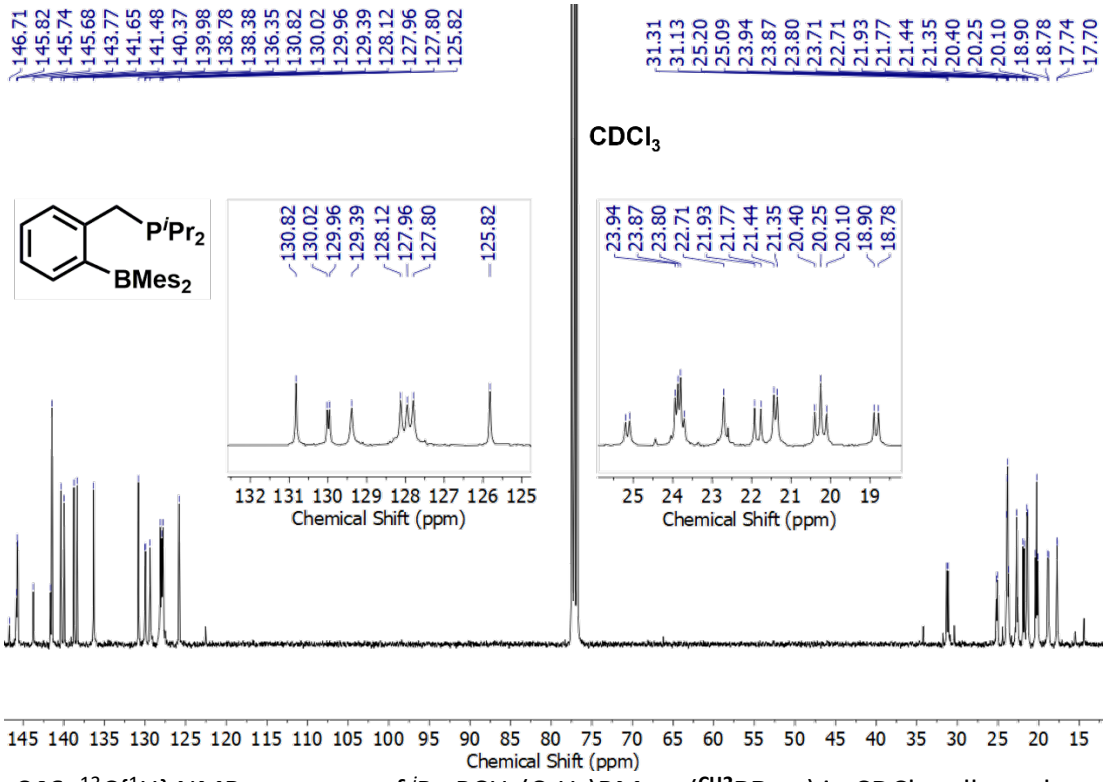

Figure S46. $^{13}C\{^{1}H\}$ NMR spectrum of $^{i}Pr_2PCH_2(C_6H_4)BMes_2$ ($^{CH2}PB_{Mes}$) in $CDCl_3$ collected at -40 °C.

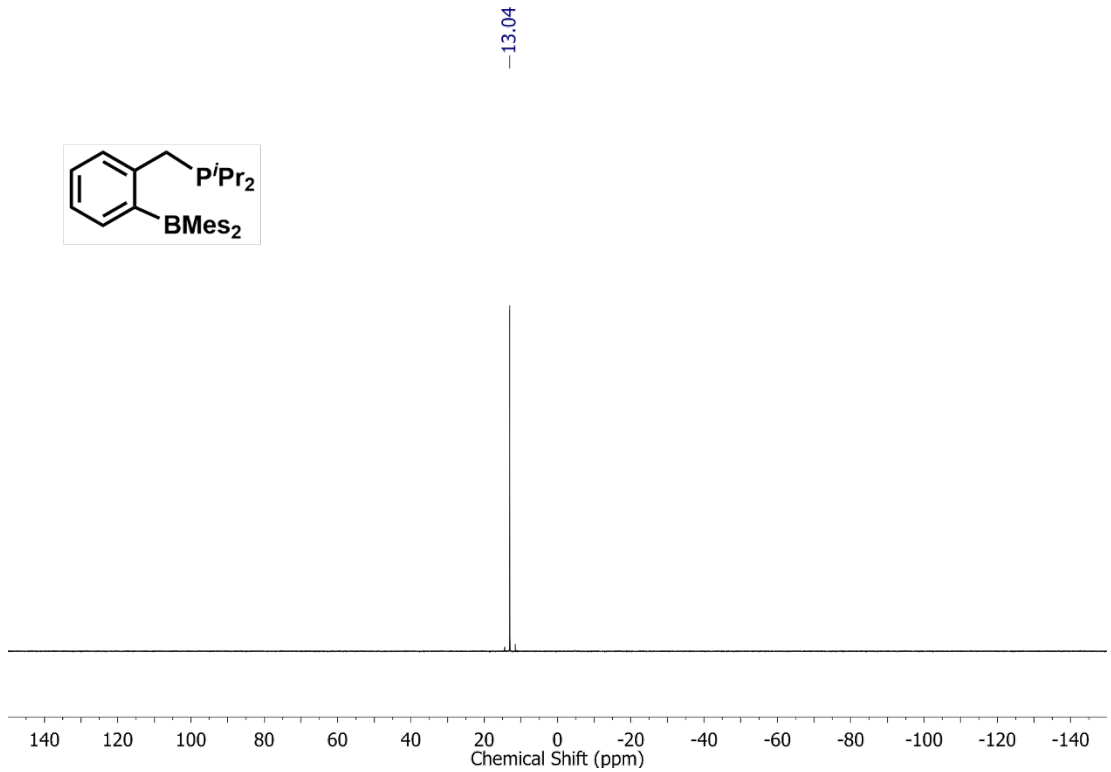

Figure S47. $^{31}P\{^1H\}$ NMR spectrum of $^{i}Pr_2PCH_2(C_6H_4)BMes_2$ ($^{CH2}PB_{Mes}$) in $CDCl_3$ collected at -40 °C.

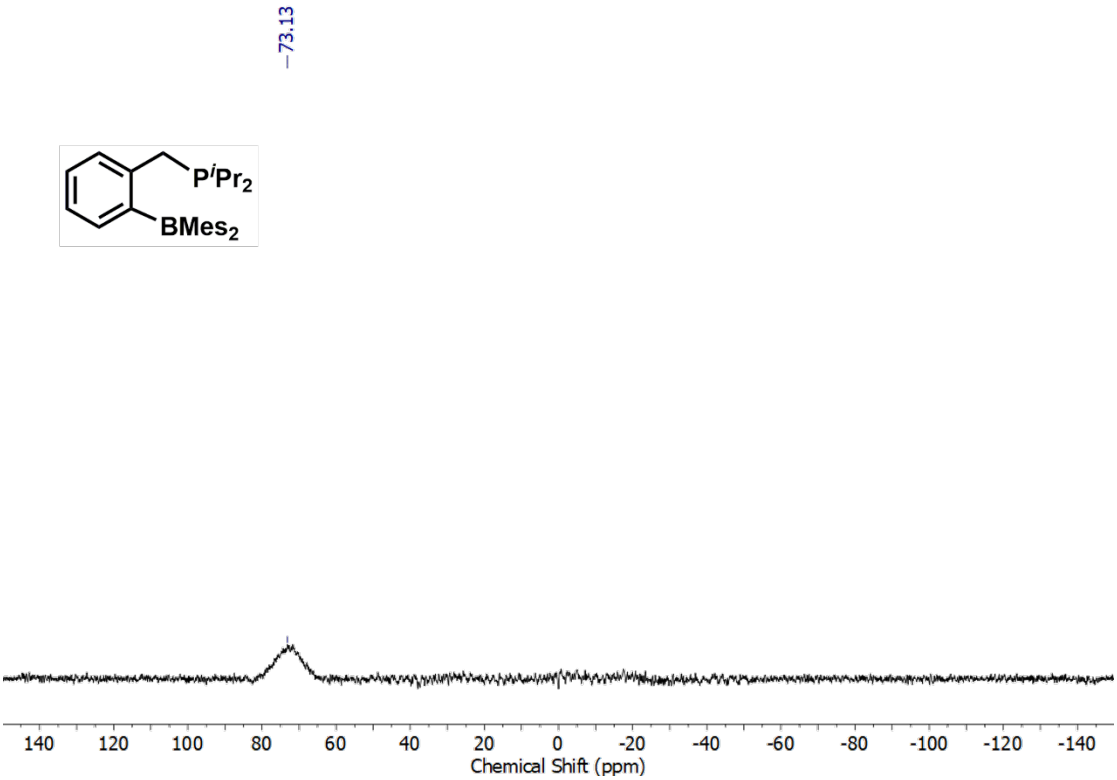

Figure S48. $^{11}B\{^1H\}$ NMR spectrum of $^{i}Pr_2PCH_2(C_6H_4)BMes_2$ ($^{CH2}PB_{Mes}$) in $CDCl_3$ collected at 25 °C.

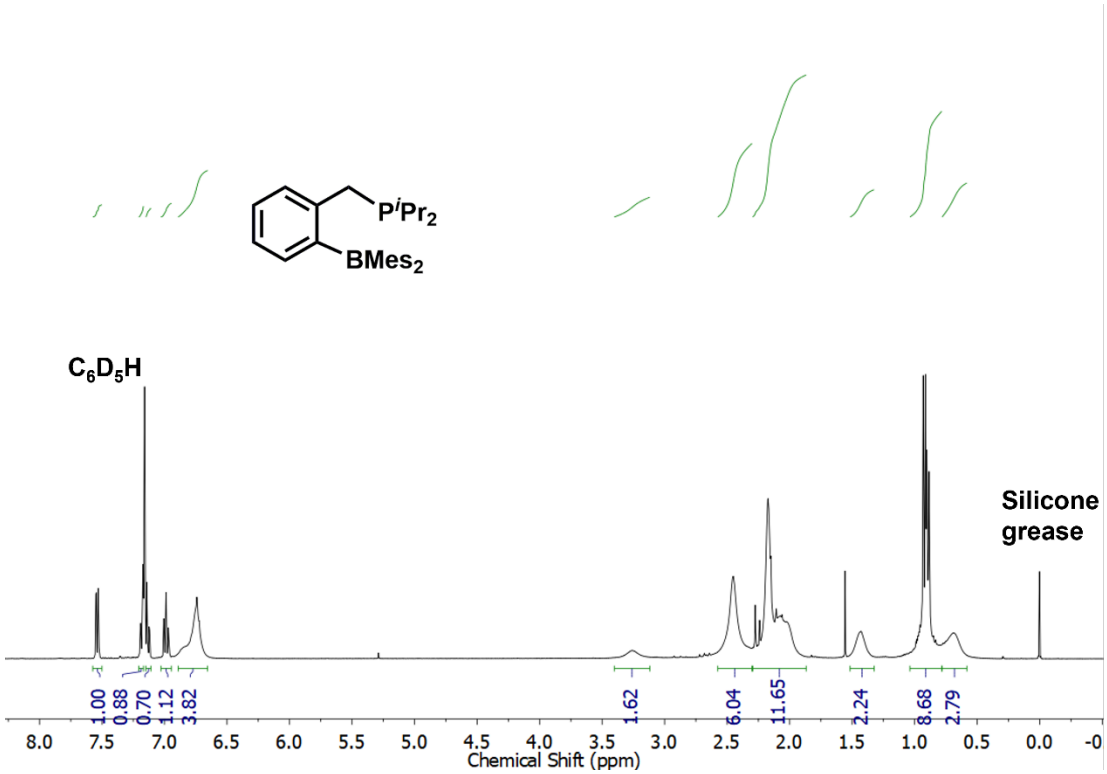

Figure S49. ^{1}H NMR spectrum of $^{i}Pr_2PCH_2(C_6H_4)BMes_2$ (**^{CH2}PB$_{Mes}$**) in C_6D_6 collected at 25 °C.

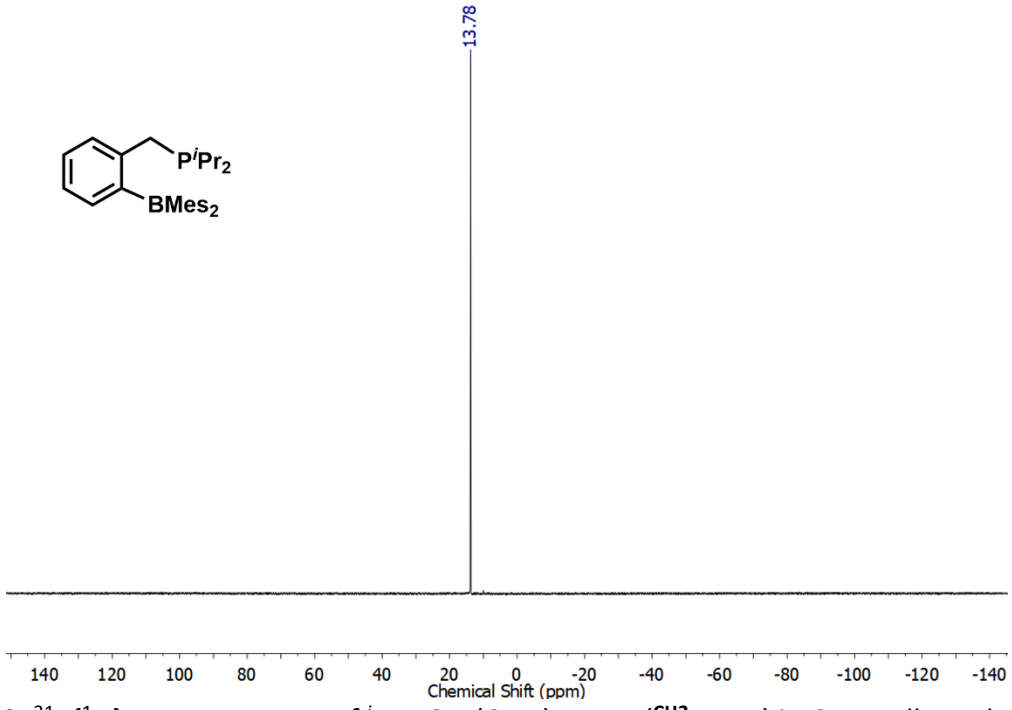

Figure S50. ^{31}P{^{1}H} NMR spectrum of $^{i}Pr_2PCH_2(C_6H_4)BMes_2$ (**^{CH2}PB$_{Mes}$**) in C_6D_6 collected at 25 °C.

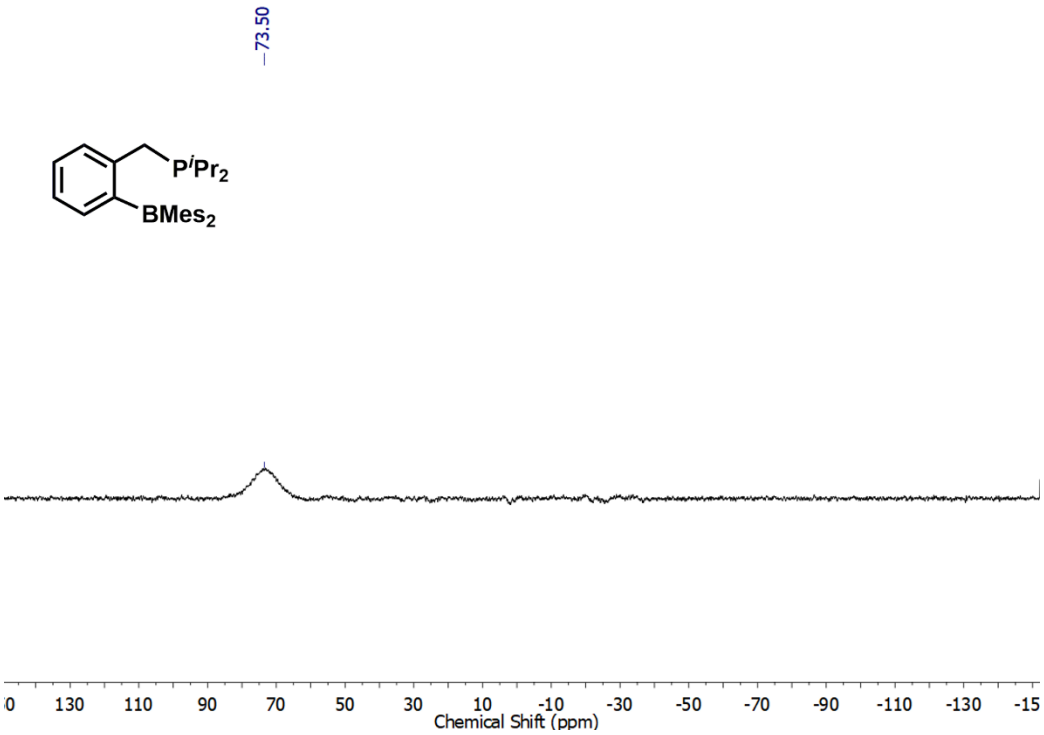

Figure S51. $^{11}B\{^1H\}$ NMR spectrum of ^{i}Pr$_2$PCH$_2$(C$_6$H$_4$)BMes$_2$ (**^{CH2}PB$_{Mes}$**) in C$_6$D$_6$ collected at 25 °C.

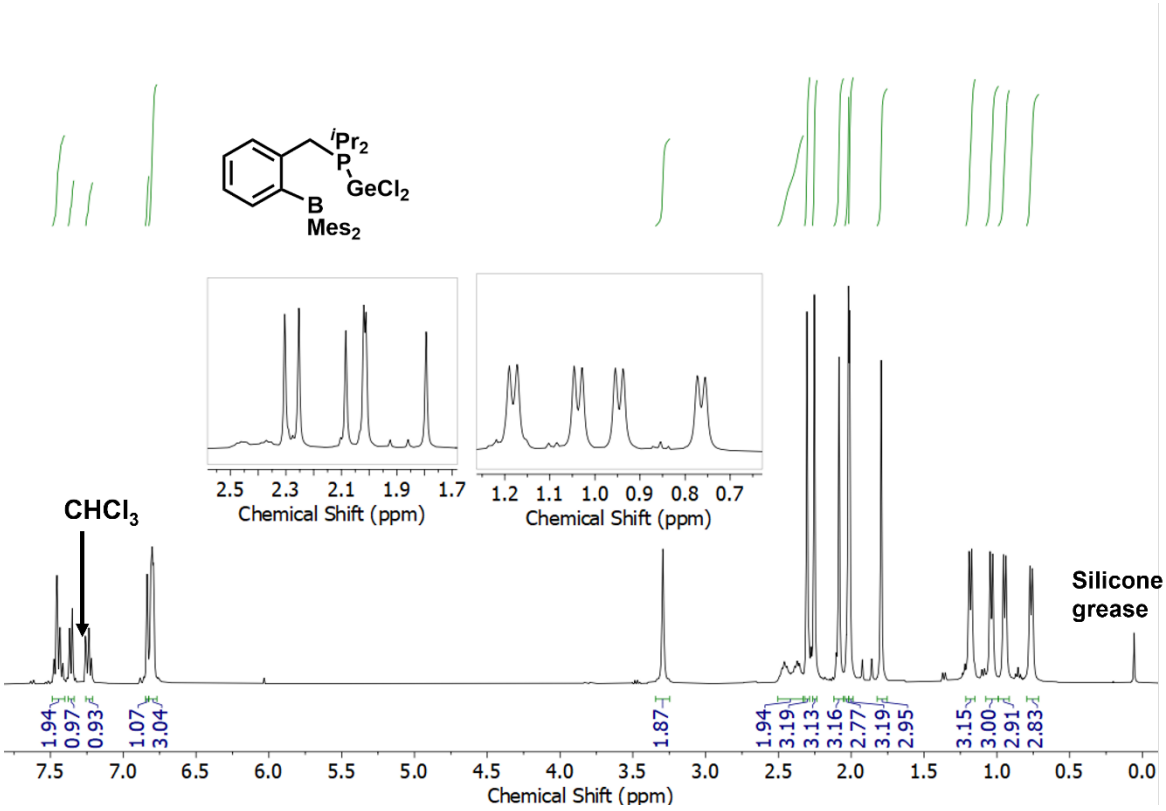

Figure S52. $^1H\{^{31}P\}$ NMR spectrum of [^{i}Pr$_2$PCH$_2$(C$_6$H$_4$)BMes$_2${GeCl$_2$}] (**11**) in CDCl$_3$ collected at -40 °C.

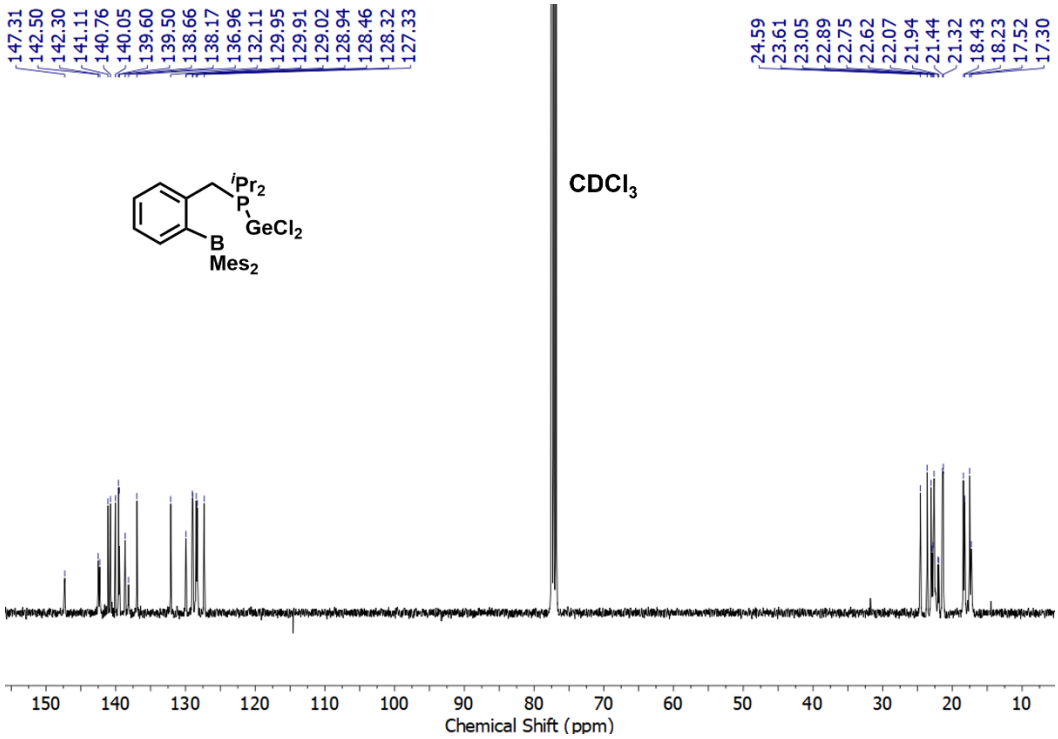

Figure S53. $^{13}C\{^{1}H\}$ NMR spectrum of [$^{i}Pr_2PCH_2(C_6H_4)BMes_2\{GeCl_2\}$] (**11**) in $CDCl_3$ collected at -40 °C.

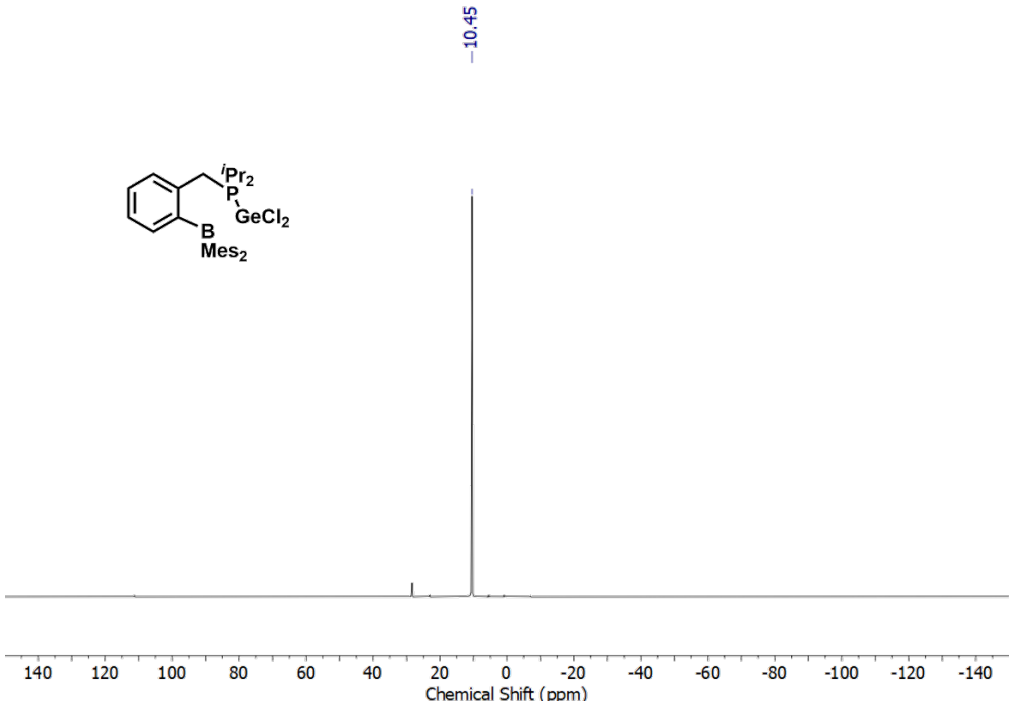

Figure S54. $^{31}P\{^{1}H\}$ NMR spectrum of [$^{i}Pr_2PCH_2(C_6H_4)BMes_2\{GeCl_2\}$] (**11**) in $CDCl_3$ collected at -40 °C. The ^{31}P resonance near 28 ppm has been tentatively assigned as [$^{i}Pr_2PCH_2(C_6H_4)BMes_2\{HCl\}$] from protonolysis of $^{CH2}\mathbf{PB}_{\mathbf{Mes}}$, since the peak appears as a doublet in the ^{31}P NMR spectrum.

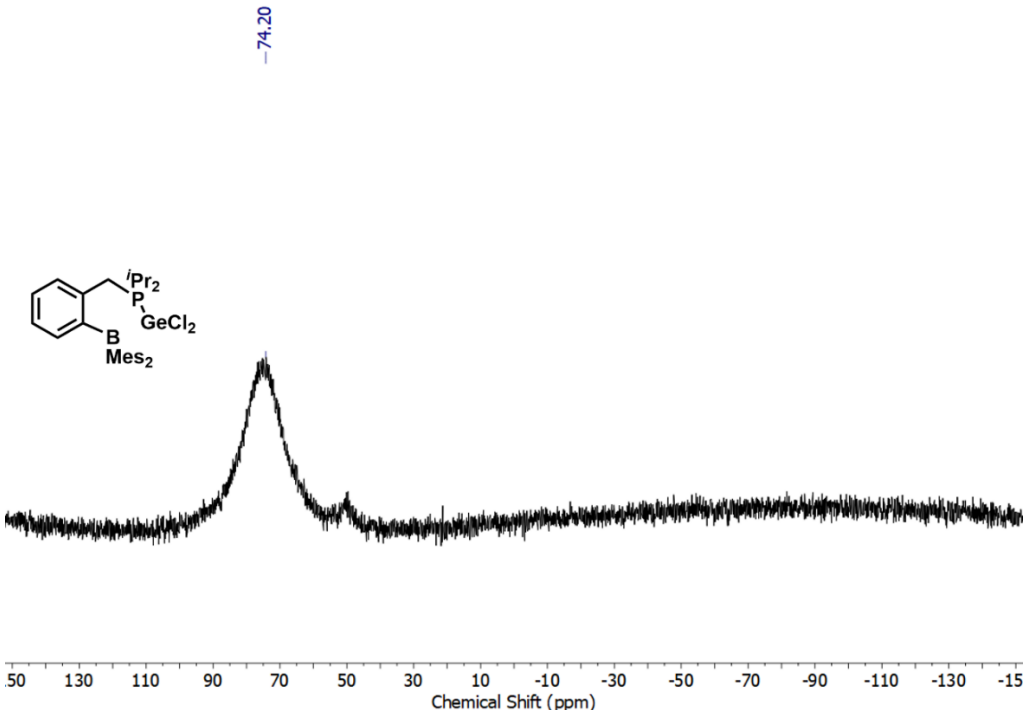

Figure S55. $^{11}B\{^{1}H\}$ NMR spectrum of [$^{i}Pr_2PCH_2(C_6H_4)BMes_2\{GeCl_2\}$] (**11**) in $CDCl_3$ collected at -40 °C.

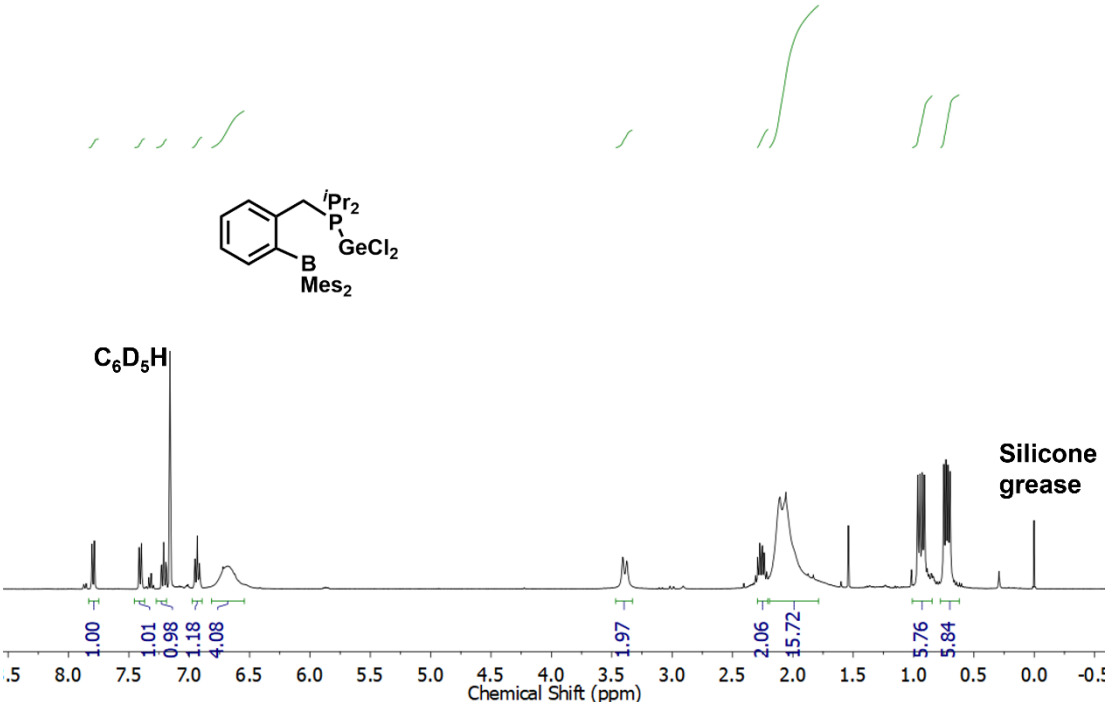

Figure S56. ^{1}H NMR spectrum of [$^{i}Pr_2PCH_2(C_6H_4)BMes_2\{GeCl_2\}$] (**11**) in C_6D_6 at 25 °C. Note that the integration of the Mes-C*H*$_3$ (m, 1.87-2.19) is often undercalculated at 16H (instead of 18H) due to significant broadening.

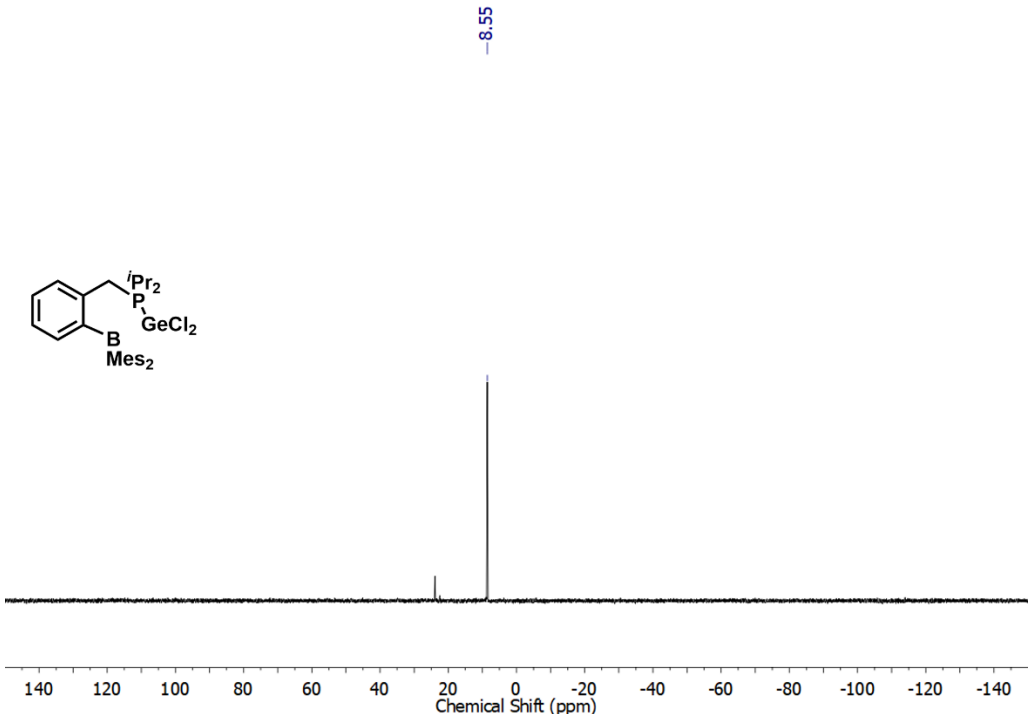

Figure S57. $^{31}P\{^{1}H\}$ NMR spectrum of [$^{i}Pr_2PCH_2(C_6H_4)BMes_2\{GeCl_2\}$] (**11**) in C_6D_6 at 25 °C.

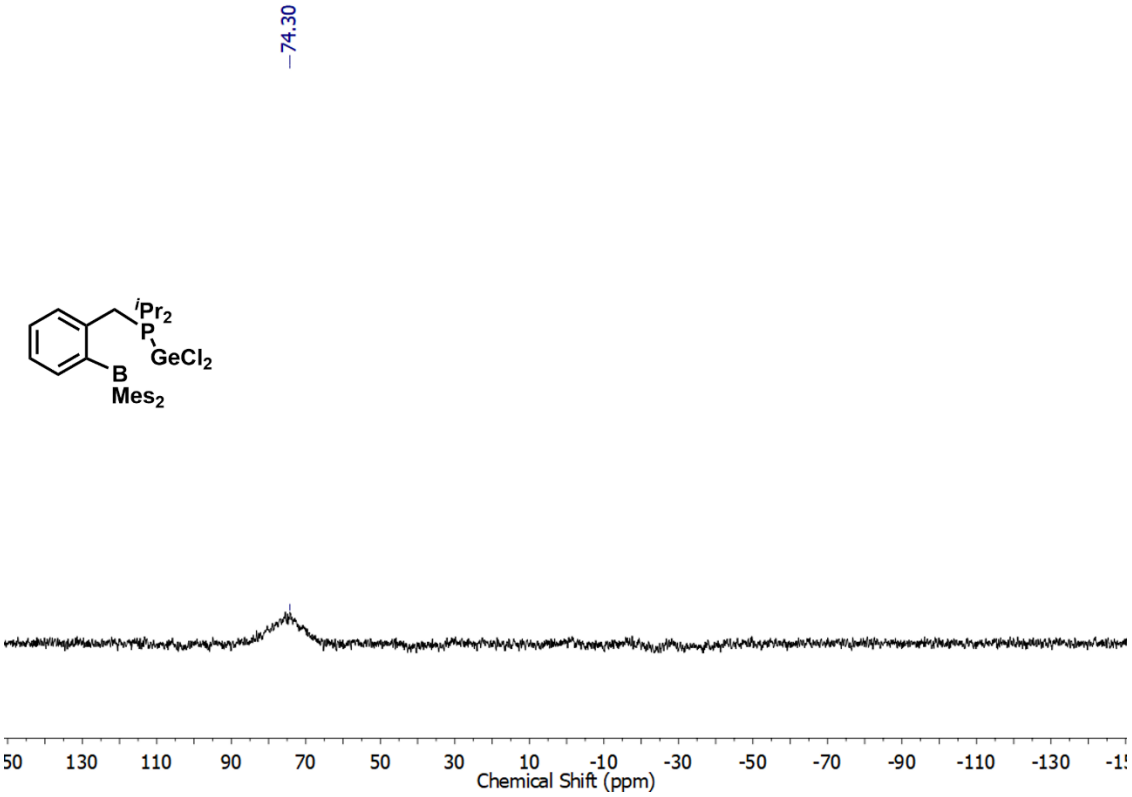

Figure S58. $^{11}B\{^{1}H\}$ NMR spectrum of [$^{i}Pr_2PCH_2(C_6H_4)BMes_2\{GeCl_2\}$] (**11**) in C_6D_6 at 25 °C.

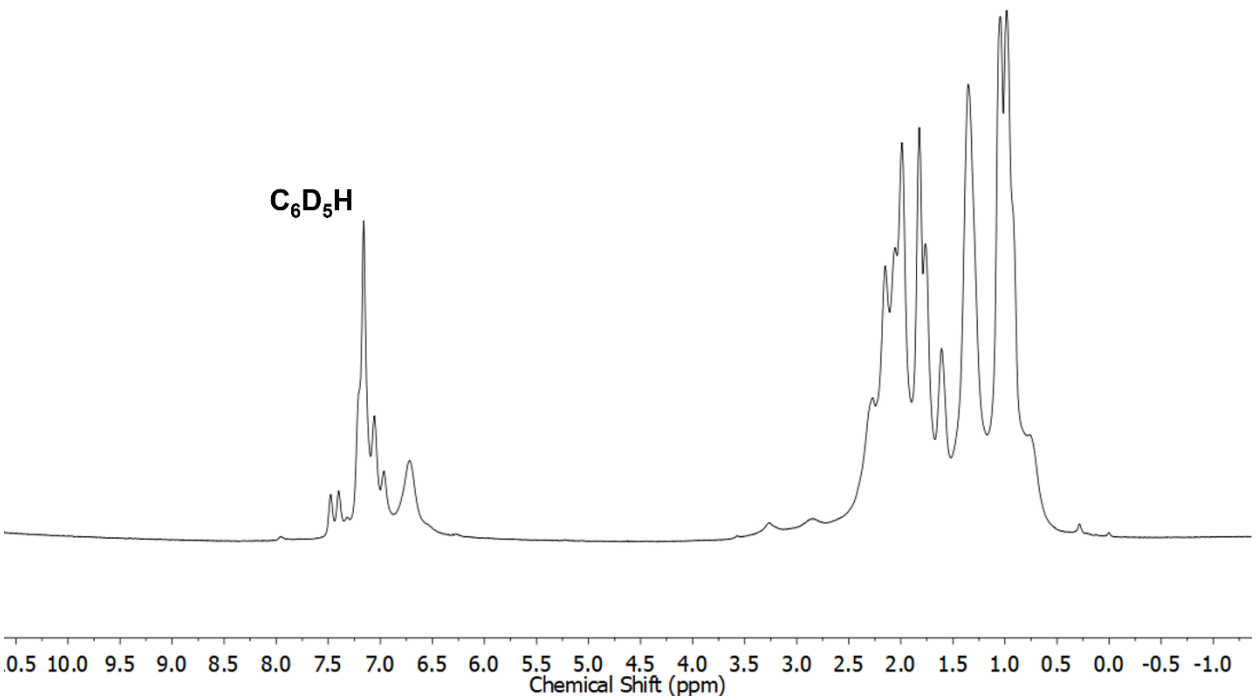

Figure S59. ^{1}H NMR spectrum of the crude reaction mixture from the combination of [^{i}Pr$_2$PCH$_2$(C$_6$H$_4$)BMes$_2${GeCl$_2$}] (**11**) with **PB** in C$_6$D$_6$. The ^{1}H NMR data is not consistent with that of free **11**, **PB**, [PB{GeCl$_2$}][S7] or **^{CH2}PB$_{Mes}$**, thus an equilibrium mixture is likely present.

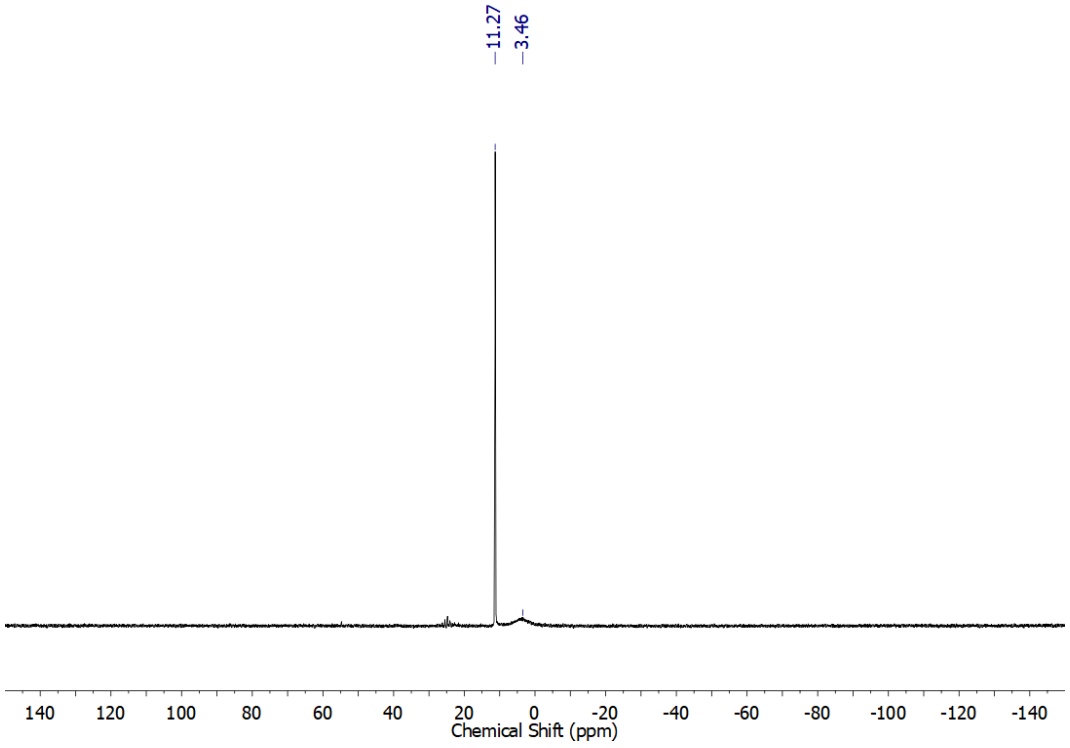

Figure S60. ^{31}P{^{1}H} NMR spectrum of the crude reaction mixture from the combination of [^{i}Pr$_2$PCH$_2$(C$_6$H$_4$)BMes$_2${GeCl$_2$}] (**11**) with **PB** in C$_6$D$_6$.

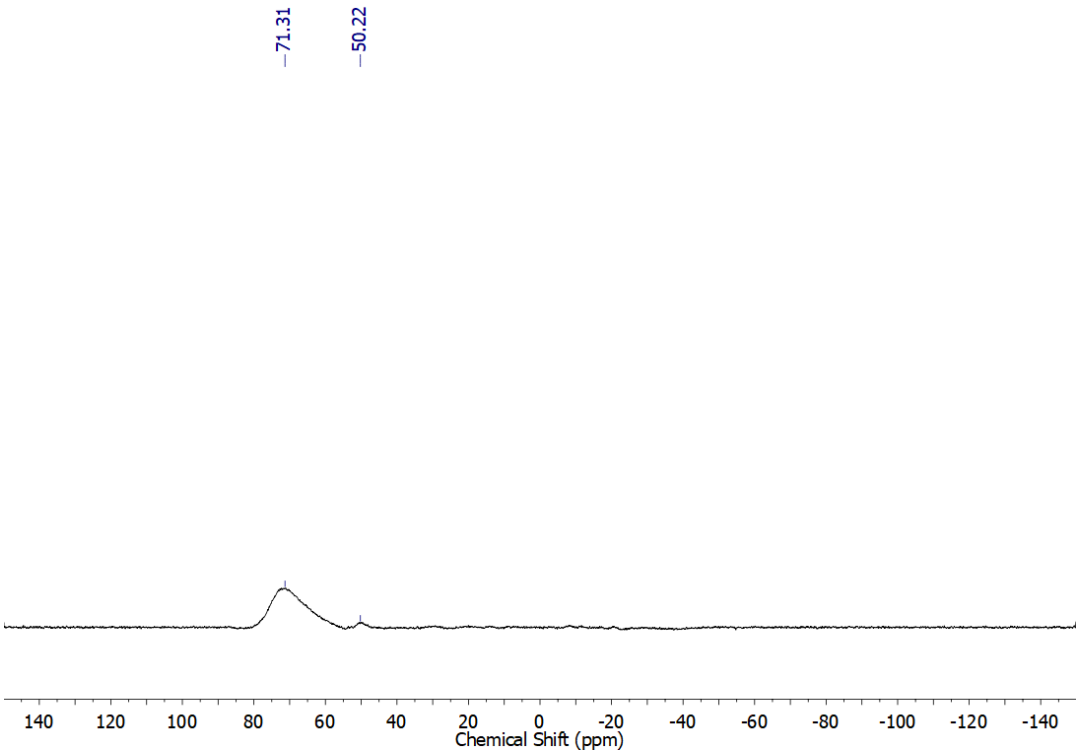

Figure S61. $^{11}B\{^{1}H\}$ NMR spectrum of the crude reaction mixture from the combination of [$^{i}Pr_2PCH_2(C_6H_4)BMes_2\{GeCl_2\}$] (**11**) with **PB** in C_6D_6.

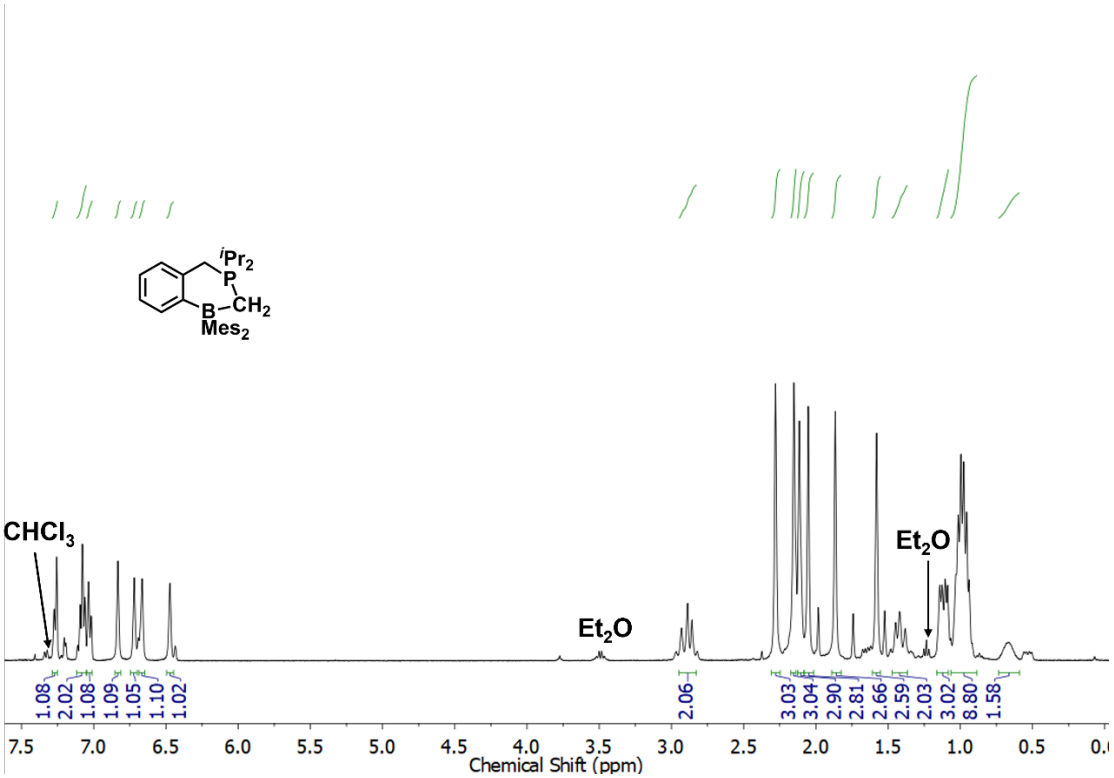

Figure S62. ^{1}H NMR spectrum of [$^{i}Pr_2PCH_2(C_6H_4)BMes_2\{CH_2\}$] (**13**) in $CDCl_3$ collected at -60 °C.

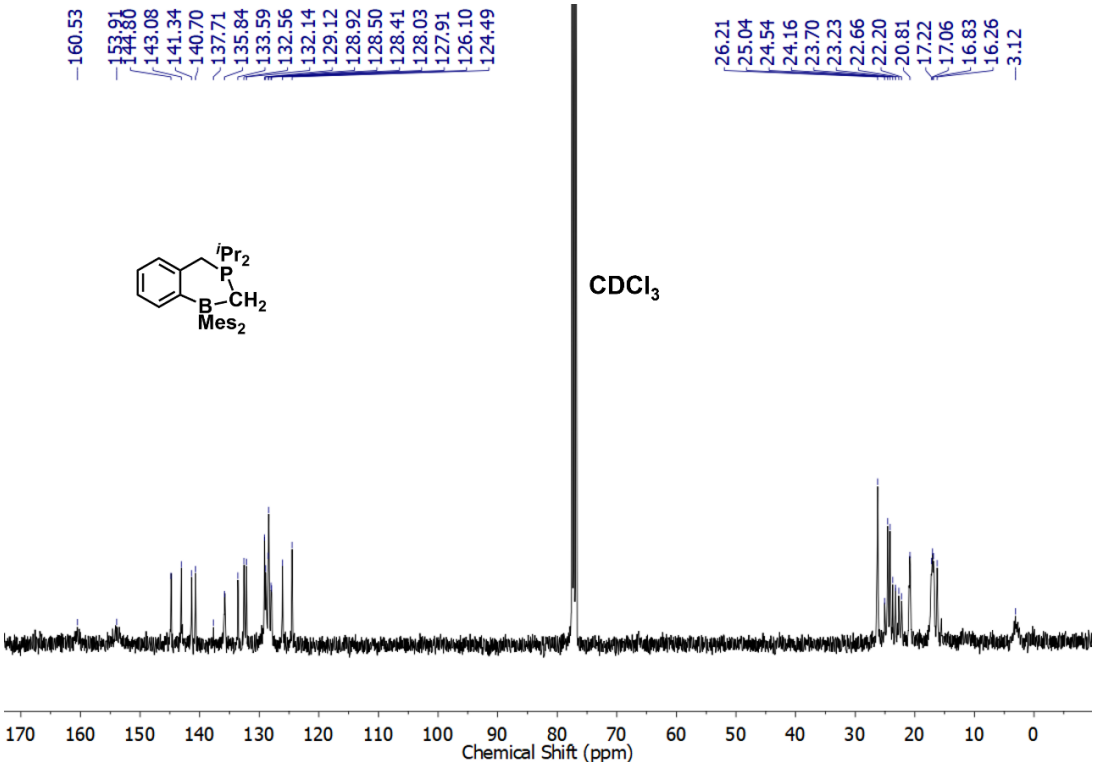

Figure S63. $^{13}C\{^{1}H\}$ NMR spectrum of [$^{i}Pr_2PCH_2(C_6H_4)BMes_2\{CH_2\}$] (**13**) in $CDCl_3$ collected at -60 °C.

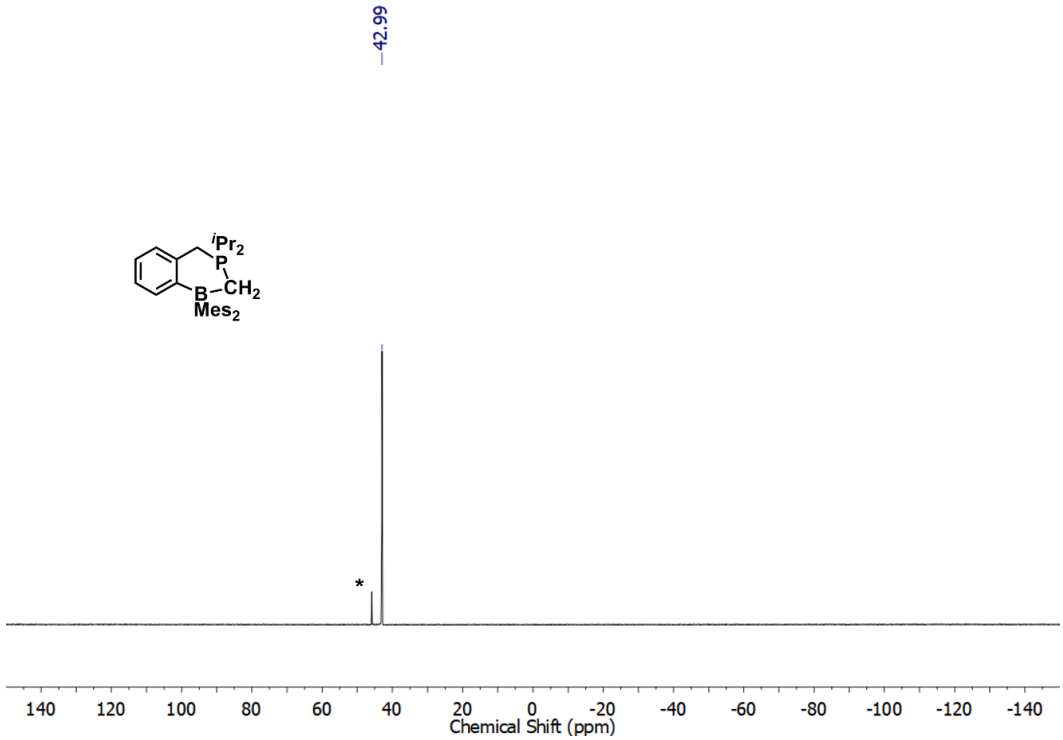

Figure S64. $^{31}P\{^{1}H\}$ NMR spectrum of [$^{i}Pr_2PCH_2(C_6H_4)BMes_2\{CH_2\}$] (**13**) in $CDCl_3$ collected at 25 °C. The ^{31}P resonance labelled with an asterisk (*) is a minor [$^{i}Pr_2PCH_2(C_6H_4)BMes_2\{MeOTf\}$] impurity, the identity of which was confirmed upon multinuclear (^{1}H, $^{31}P\{^{1}H\}$, $^{11}B\{^{1}H\}$, $^{19}F\{^{1}H\}$) NMR spectroscopy tracking of the reaction mixture between $^{CH2}\mathbf{PB}_{\mathbf{Mes}}$ and MeOTf over time.

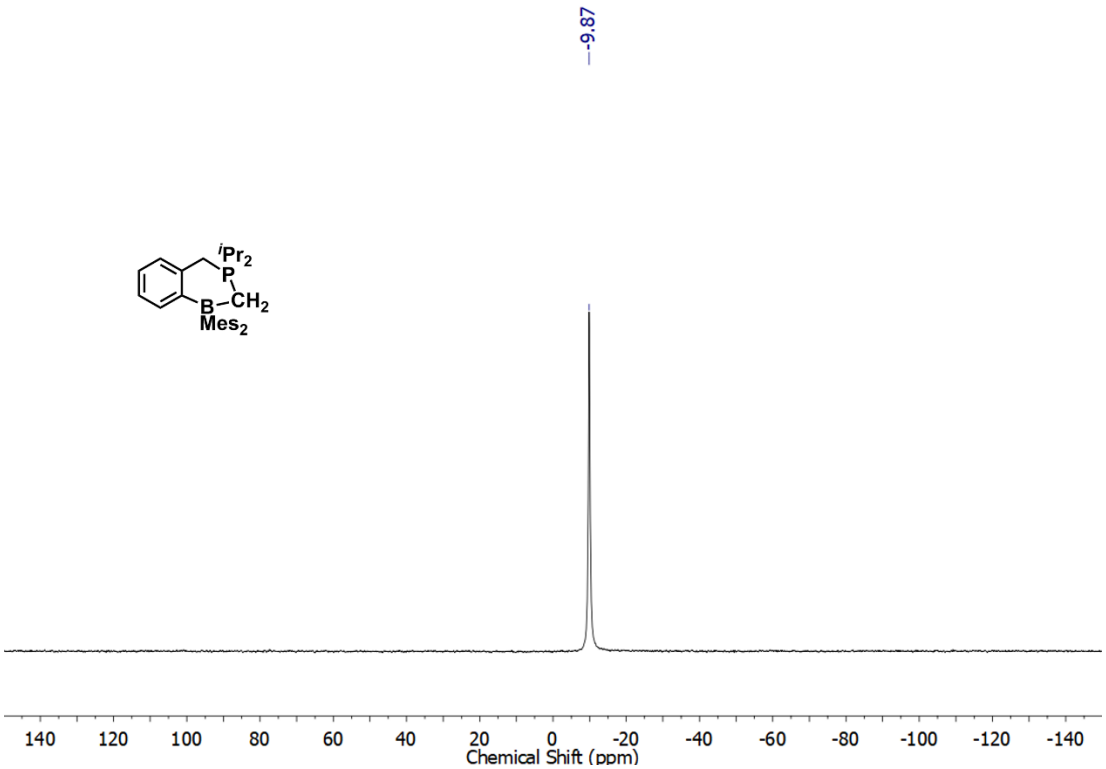

Figure S65. $^{11}B\{^{1}H\}$ NMR spectrum of [$^{i}Pr_2PCH_2(C_6H_4)BMes_2\{CH_2\}$] (**13**) in $CDCl_3$ collected at 25 °C.

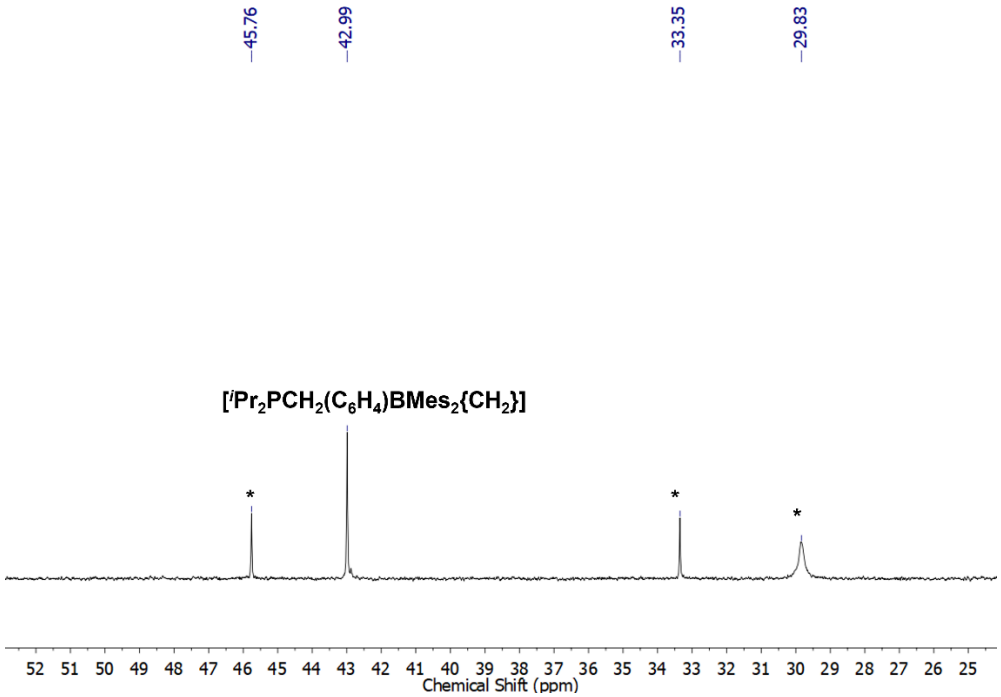

Figure S66. $^{31}P\{^{1}H\}$ NMR spectrum of the crude reaction mixture from the combination of [$^{i}Pr_2PCH_2(C_6H_4)BMes_2\{CH_2\}$] (**13**) with $^{n}BuLi$ in C_6D_6. Peaks labelled with an asterisk (*) are unknown.

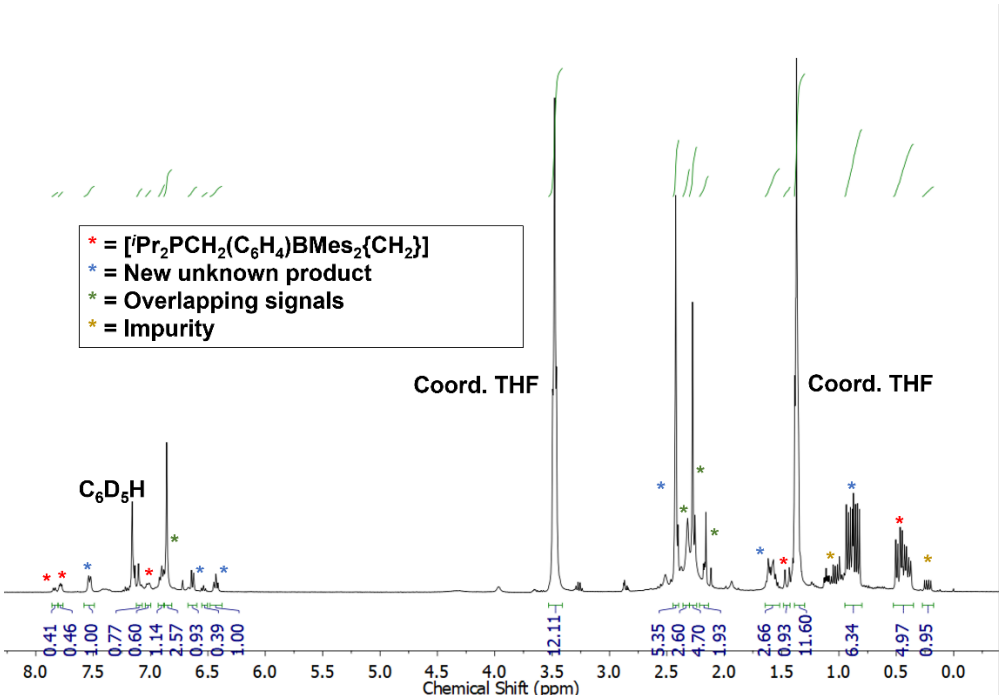

Figure S67. ^{1}H NMR spectrum of the crude reaction mixture from the combination of [^{i}Pr$_2$PCH$_2$(C$_6$H$_4$)BMes$_2${CH$_2$}] (**13**) with ^{n}BuLi in C$_6$D$_6$. ^{1}H integration was performed between the ArH resonance at 7.78 ppm (pseudo-t, for **13**) and 7.54 ppm (d, for unknown new product), showing 31.5 % of **13** in the reaction mixture. To obtain accurate ^{1}H NMR integrations, all peaks were linearly corrected to account for baseline fluctuations.

3. Density functional theory (DFT) computations

Structure geometries were optimized in the gas phase using the M06-2X[S8] functional and the cc-pVTZ[S9] basis set using Gaussian16.[S10] Frequency analyses were performed to confirm the presence of no imaginary frequencies for ground states. Optimized geometries and orbitals were rendered using VMD.[S11] NBO analysis was performed at the M06-2X/cc-pVTZ level of theory using the NBO 6.0 program.[S12]

To obtain an estimate of the collective P–E and B–E bond strengths within our FLP-stabilized $SiCl_2$, $SiBr_2$, and $GeCl_2$ adducts, computations were performed on the release of singlet[S13] EX_2 (E = Si, Ge; X = Cl, Br) from **1**, **2** and **5** in the gas phase.† The free energy of activation ($\Delta G^{\ddagger}$) associated with EX_2 loss cannot be discussed at this time since transition states for P–E/E–B bond scission could not be located. For both **1** and **5**, the propensity to release singlet[S13] SiX_2 (X = Cl for **1**, Br for **5**) and generate free **PB** appears to be identical in magnitude and endoergic (ΔG) by 20.3 kcal mol^{-1}, respectively, in the gas phase (computations at a M06-2X/cc-pVTZ level of theory; Eqn. S1). It is expected that the P–Ge and Ge–B bonds in [PB{$GeCl_2$}] (**2**) should be easier to break versus the P–Si and Si–B linkages in [PB{$SiCl_2$}] (**1**). Accordingly, the free energy penalty (ΔG) associated with the release of singlet $GeCl_2$ from [PB{$GeCl_2$}] (**2**) was computed to be lower than the loss of SiX_2 from either **1** or **5** by 8.4 kcal mol^{-1} (Eqn. S2).

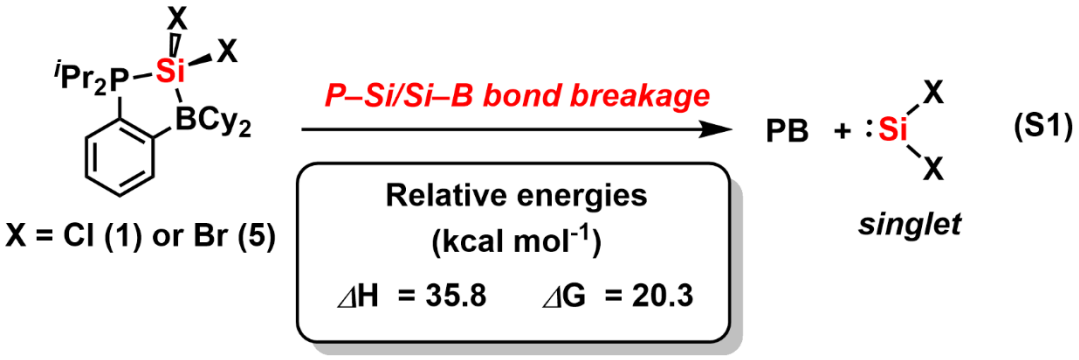

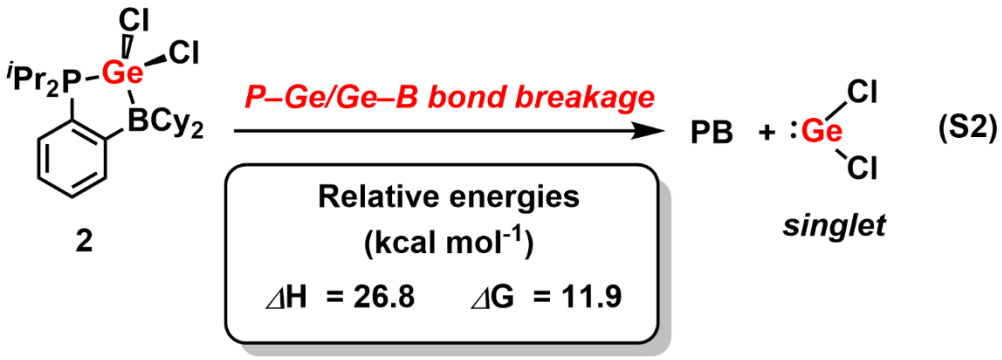

All attempts to optimize [PB{C}] in a singlet ground state (at the M06-2X/cc-pVTZ level of theory) converged into a 1,3-cyclohexyl shift product, [^{i}Pr$_2$P(C$_6$H$_4$)BCy{CCy}]; however, by using the optimized geometry of the triplet [PB{C}] and running a frequency optimization as a singlet, the total energy of the singlet [PB{C}] complex was obtained. The triplet ground state of [PB{C}] could be optimized and the triplet structure of [PB{C}] is included below (Fig. S69). The triplet [PB{C}] structure is lower in Gibbs free energy by 16.8 kcal mol^{-1} than the singlet [PB{C}] structure (Figs. S69 and S70). The 1,3-cyclohexyl shift product, [^{i}Pr$_2$P(C$_6$H$_4$)BCy{CCy}], is lower in free energy by 76.7 kcal mol^{-1} compared to the triplet [PB{C}] structure (Figs. S68 and S70). Both the *cis*- and *trans*- structures of [PB{C=C}PB] were computationally optimized as singlet ground states at a M06-2X/cc-pVTZ level of theory. Energetically, the *trans*-[PB{C=C}PB] structure was favored by -20.9 kcal mol^{-1} in Gibbs free energy over the *cis*-[PB{C=C}PB structure (Fig. S71).

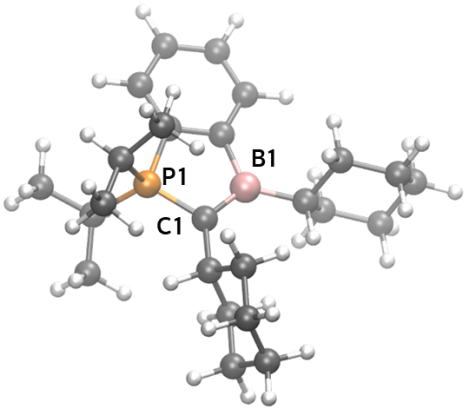

Bond	Calculated
P1–C1	1.727
C1–B1	1.486

Bond	WBI	Atom	Q_{NPA}
P1–C1	1.08	P1	1.65
C1–B1	1.29	C1	0.96
-	-	B1	0.71

Figure S68. Optimized [^{i}Pr$_2$P(C$_6$H$_4$)BCy{CCy}] structure (at the M06-2X/cc-pVTZ level of theory) with selected bond lengths (Å), Wiberg bond indices (WBI) and natural charges (Q_{NPA}).

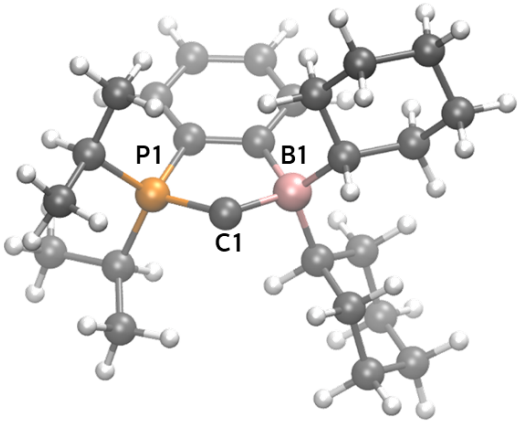

Bond	Calculated
P1–C1	1.748
C1–B1	1.638

Bond	WBI	Atom	Q_{NPA}
P1–C1	1.10	P1	1.44
C1–B1	0.94	C1	-0.27
-	-	B1	0.27

Figure S69. Optimized triplet ground state of [PB{C}] (at the M06-2X/cc-pVTZ level of theory) with selected bond lengths (Å), Wiberg bond indices (WBI) and natural charges (Q_{NPA}).

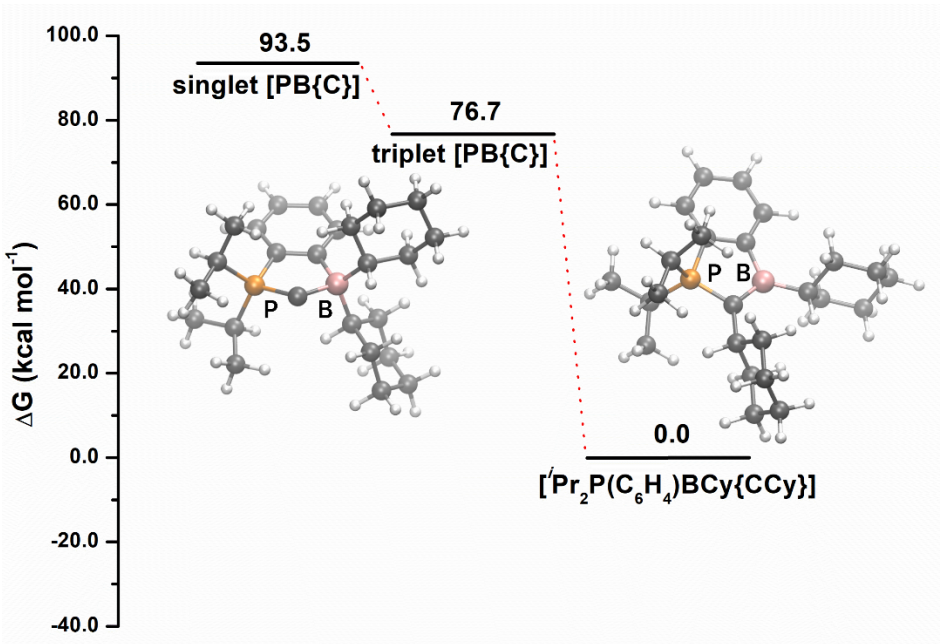

Figure S70. Optimized structures of [PB{C}] (singlet and triplet states) and [^{i}Pr$_2$P(C$_6$H$_4$)BCy{CCy} (at the M06-2X/cc-pVTZ level of theory) on a Gibbs free energy diagram (kcal mol^{-1}).

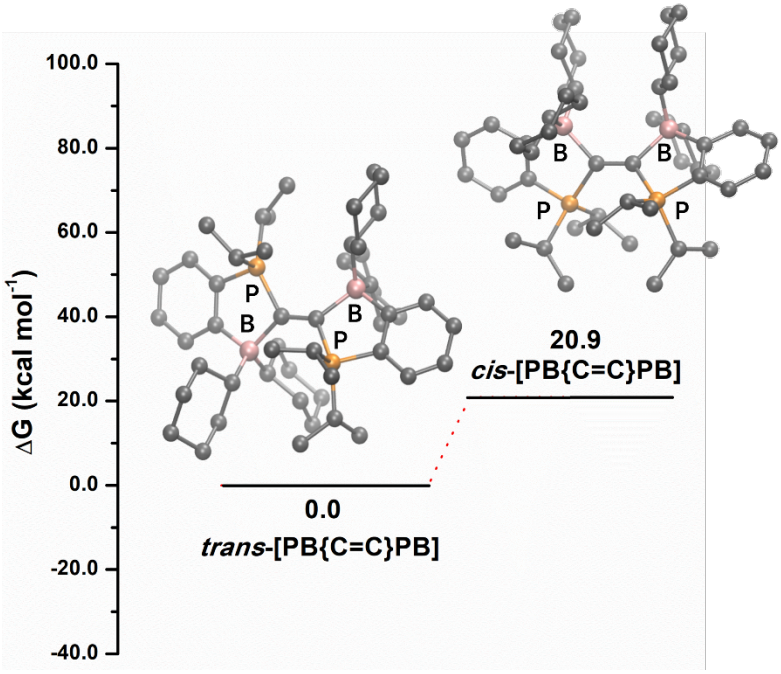

Figure S71. Optimized structures of [PB{C=C}PB] (singlet ground state; at the M06-2X/cc-pVTZ level of theory) on a Gibbs free energy diagram (kcal mol^{-1}). All hydrogens have been removed for clarity.

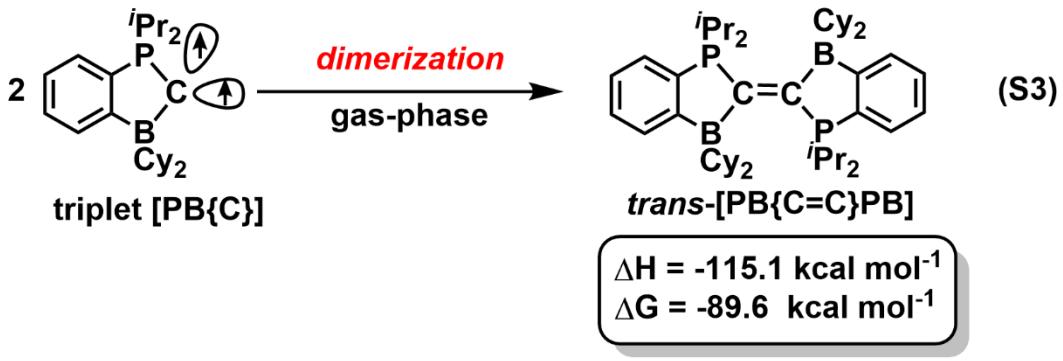

(S3)

The enthalpy and Gibbs free energy of the dimerization reaction (shown as Eqn. S3 above) were computed to be -115.1 and -89.6 kcal/mol, respectively.

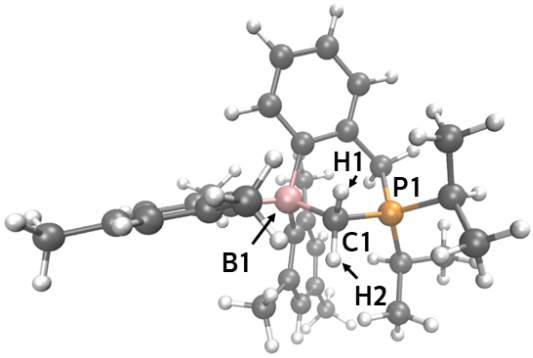

Bond	Calculated	Experimental
P1–C1	1.7776	1.7617(19)
C1–B1	1.7166	1.702(3)

Bond	WBI	Atom	Q_{NPA}
P1–C1	0.98	P1	1.70
C1–B1	0.75	B1	0.49
C1–H1	0.89	C1	-1.05
-	-	H1	0.26

Figure S72. Optimized [$^{i}Pr_2PCH_2(C_6H_4)BMes_2\{CH_2\}$] structure (at the M06-2X/cc-pVTZ level of theory) with selected bond lengths (Å), Wiberg bond indices (WBI) and natural charges (Q_{NPA}).

4. References

S1. R. H. Blessing, *Acta Cryst.*, 1995, **A51**, 33–38.
S2. G. M. Sheldrick, *Acta Cryst.*, 2015, **A71**, 3–8.
S3. G. M. Sheldrick, *Acta Cryst.*, 2015, **C71**, 3–8.
S4. O. V. Dolomanov, L. J. Bourhis, R. J. Gildea, J. A. K. Howard and H. Puschmann, *J. Appl. Cryst.*, 2009, **42**, 339–341.
S5. A. C. Filippou, O. Chernov and G. Schnakenburg, *Angew. Chem., Int. Ed.*, 2009, **48**, 5687–5690.
S6. S. Aime, R. K. Harris, E. M. McVicker, and M. Fild, *J. Chem. Soc., Dalton Trans.,* 1976, 2144–2153.
S7. A. A. Omaña, R. K. Green, R. Kobayashi, Y. He, E. R. Antoniuk, M. J. Ferguson, Y. Zhou, J. G. C. Veinot, T. Iwamoto, A. Brown and E. Rivard, *Angew. Chem., Int. Ed.*, 2021, **60**, 228–231.
S8. Y. Shao and D. Truhlar, *Theor. Chem. Acc.*, 2008, **120**, 215–241.
S9. T. H. Dunning Jr., *J. Chem. Phys.*, 1989, **90**, 1007–1023.
S10. M. J. Frisch, G. W. Trucks, H. B. Schlegel, G. E. Scuseria, M. A. Robb, J. R. Cheeseman, G. Scalmani, V. Barone, G. A. Petersson, H. Nakatsuji, X. Li, M. Caricato, A. V. Marenich, J. Bloino, B. G. Janesko, R. Gomperts, B. Mennucci, H. P. Hratchian, J. V. Ortiz, A. F. Izmaylov, J. L. Sonnenberg, D. Williams-Young, F. Ding, F. Lipparini, F. Egidi, J. Goings, B. Peng, A. Petrone, T. Henderson, D. Ranasinghe, V. G. Zakrzewski, J. Gao, N. Rega, G. Zheng, W. Liang, M. Hada, M. Ehara, K. Toyota, R. Fukuda, J. Hasegawa, M. Ishida, T. Nakajima, Y. Honda, O. Kitao, H. Nakai, T. Vreven, K. Throssell, J. A. Montgomery, Jr., J. E. Peralta, F. Ogliaro, M. J. Bearpark, J. J. Heyd, E. N. Brothers, K. N. Kudin, V. N. Staroverov, T. A. Keith, R. Kobayashi, J. Normand, K. Raghavachari, A. P. Rendell, J. C. Burant, S. S. Iyengar, J. Tomasi, M. Cossi, J. M. Millam, M. Klene, C. Adamo, R. Cammi, J. W. Ochterski, R. L. Martin, K. Morokuma, O. Farkas, J. B. Foresman and D. J. Fox, *Gaussian 16*, Revision A. 03, Gaussian Inc., Wallingford CT, 2016.
S11. W. Humphrey, A. Dalke and K. Schulten, *J. Mol. Graphics*, 1996, **14**, 33–38.
S12. E. D. Glendening, J. K. Badenhoop, A. E. Reed, J. E. Carpenter, J. A. Bohmann, C. M. Morales, C. R. Landis and F. Weinhold, *NBO 6.0*, Theoretical Chemistry Institute, University of Wisconsin, Madison WI, 2013.
S13. (*a*) J. L. Berkowitz, J. P. Green, H. Cho and R. Ruscic, *J. Chem. Phys.*, 1987, **86**, 1235–1248; (*b*) Y. Apeloig, R. Pauncz, M. Karni, R. West, W. Steiner and D. Chapman, *Organometallics*, 2003, **22**, 3250–3256; (*c*) S. K. Shin, W. A. Goddard III and J. L. Beauchamp, *J. Phys. Chem.*, 1990, **94**, 6963–6969; (*d*) J.-C. Barthelat, B. S. Roch, G. Trinquier and J. Satgé, *J. Am. Chem. Soc.*, 1980, **102**, 4080–4085.